High-temperature high-pressure calorimetry for studying thermochemical energy storage materials

by

Ke Hu

B.A.Sc., University of British Columbia, 2015

A THESIS SUBMITTED IN PARTIAL FULFILLMENT OF THE REQUIREMENTS FOR THE DEGREE OF

MASTER OF APPLIED SCIENCE

in

The Faculty of Graduate and Postdoctoral Studies

(Chemical and Biological Engineering)

THE UNIVERSITY OF BRITISH COLUMBIA

(Vancouver)

September 2019

The following individuals certify that they have read, and recommend to the Faculty of Graduate and Postdoctoral Studies for acceptance, the thesis entitled:

High-temperature high-pressure calorimetry for studying thermochemical energy storage materials

submitted by Ke Hu in partial fulfillment of the requirements for

the degree of Master of Applied Science

in Chemical and Biological Engineering

Examining Committee:

Curtis Berlinguette

Supervisor

Anthony Wachs

Supervisory Committee Member

Vikramaditya Yadav

Supervisory Committee Member

Abstract

Metal hydrides that can hydrogenate and dehydrogenate reversibly at high-temperature and high-pressure are considered candidate materials for thermochemical energy storage (TES). The thermodynamic and kinetic properties of these metal hydrides are poorly defined due to the limitation of the measurement techniques at high-temperature and high pressure. This thesis describes a custom-designed high-temperature and high-pressure calorimeter for studying gram-scale heterogeneous chemical reactions that expands the limits of TES research. Chapter 2 outlines the physical design and fabrication details of the calorimeter. The calorimeter was demonstrated operating up to at least 1232 °C while under pure hydrogen pressures up to 33 bar with simultaneous in-situ calorimetric and pressure measurements. A finite element analysis (FEA) model was constructed using COMSOL Multiphysics to aid the experimental design. Chapter 3 outlines a thermal analysis algorithm that is modelled with a lumped-element model. The chemical enthalpy can be estimated using this algorithm along with the power and temperature profile data from this calorimeter. The model was verified using an aluminum heat of fusion experiment, as well as an exothermic process simulation to obtain a fitting accuracy of over 99%. Chapter 4 summarizes this work and offers future directions of the research that can be conducted using this instrument.

Lay summary

The objective of the thesis is to introduce a custom-designed calorimeter that is able to operate at high-temperature and-high pressure to study thermochemical energy storage (TES) materials. TES materials are used to store excess energy during periods of high solar irradiance, and release the energy as required during periods of low to zero irradiance. The thermodynamic and kinetic data of high-temperature TES materials is lacking due to the limitation of the instruments. I have worked collaboratively to design and fabricate a novel calorimeter that is capable of operating in the high temperature and pressure regime. I also developed an algorithm that can calculate the heat change of the sample based on the measured temperatures.

Preface

This work done in this thesis was done under the supervision of Dr. Curtis P. Berlinguette.

Chapter 2 is based on work conducted in the Berlinguette Laboratory at UBC by myself and Ben P. MacLeod, Phil A. Schauer, Brian Lam and David K. Fork from Google Inc.. Ben MacLeod, Brian Lam and I were responsible for the physical design using CAD software and fabrication of the calorimeter including the heater coil, pressure vessel, isothermal cooling jacket, thermocouple positioning. Phil was responsible for the design of the control software by LabVIEW. I am also responsible for building the finite element analysis model using COMSOL. This chapter is adapted from the paper "High-Temperature High-Pressure Calorimeter for Studying Gram-Scale Heterogeneous Chemical Reactions", *Rev. Sci. Instrum.* **2017**, *88* (8), 084101.

Chapter 3 is based on my unpublished work conducted in Berlinguette Laboratory at UBC. I performed all the model design and coding in MATLAB. The collection of data that is used in the model was performed by Ben MacLeod and myself. A different model from Ben is published in the paper "High-Temperature High-Pressure Calorimeter for Studying Gram-Scale Heterogeneous Chemical Reactions", *Rev. Sci. Instrum.* **2017**, *88* (8), 084101.

I prepared the drafts of this thesis with revisions by Dr. Curtis P. Berlinguette.

Table of contents

List of tables

List of figures

List of symbols, abbreviations and nomenclature

Symbol	Definition
’	Foot
”	Inch
2D	Two dimensional
3D	Three dimensional
AC	Alternating current
Al	Aluminum
AWG	American wire gauge
C	Heat capacity
CAD	Computer-aided design
C_p	Specific heat
CSP	Concentrated solar power
DC	Direct current
DSC	Differential scanning calorimetry
FEA	Finite element analysis
Ge	Germanium
h	Planck constant
h	hour
H_2	Hydrogen gas
ID	Inner diameter
J	Joule
K	Kelvin
k	Thermal conductivity
kg	Kilogram

KNO_3	Potassium nitrate
kWh	Kilowatt-hour
L_f	Latent heat of fusion
LiH	Lithium hydride
m	Mass
m^3	Cubic meter
$Mg(BH_4)_2$	Magnesium borohydride
Mg_2FeH_6	Magnesium iron hydride
Mg_2NiH_4	Magnesium nickel hydride
MgH_2	Magnesium hydride
min	Minute
mL	Milliliter
mol	Mole
mW	Milliwatt
$NaNO_3$	Sodium nitrate
^oC	Degree Celsius
OD	Outer diameter
P	Power
Q	Heat change
Si	Silicon
Sn	Tin
T	Temperature
TES	Thermal energy storage
TGA	Thermogravimetric analysis
W	Watt
wt%	Weight percent

ΔH^0	Enthalpy change at standard state
ΔH_r	Reaction enthalpy
ΔT	Temperature change
η	efficiency
μg	Microgram
v	Frequency

Acknowledgments

I would like to express my appreciation to my supervisor Dr. Curtis P. Berlinguette. You have offered me an excellent opportunity to work in this dynamic and creative research group. Your support and patience helped me to complete this thesis.

Thank you to my defense committee members Dr. Vikramaditya G. Yadav and Dr. Anthony Wachs for their time and effort on my thesis.

I would also like to thank all the Berlinguette group members who keep offering me help and support. I would especially thank Dr. Phil Schauer, Dr. Brian Lam, Ben Macleod for being great team mates and offering guidance when I first started doing scientific research. I would also give special thanks to Dr. Wei Cheng, Caroline Krzykowski, Arthur Fink, David Dvorak, Jesse Hudkins, as colleagues and friends, for the wonderful experience working together to make the research work less stressful.

Dedication

I dedicate this thesis to my family.

Chapter 1 Introduction

1.1 Motivation for research

Solar energy can be converted to electrical energy by concentrated solar power (CSP) plants, which collect solar thermal energy and utilize it to drive power generators. The intermittent nature of solar energy necessitates the need for energy storage systems such as batteries and thermal energy storage (TES).[2] Battery based storage is commonly utilized to store electrical energy,[3,4] while TES systems, which utilize materials including molten salts, liquid metal, metal oxides, and metal hydrides,[5] are used to store thermal energy collected by CSP plants before it is converted to electricity. Battery based storage technologies typically have round trip efficiencies (the ratio between retrieved energy and input energy from the storage method[6]) lower than 80%.[3] In comparison, TES systems have higher round trip efficiencies that exceed 95% because TES directly stores solar thermal energy into chemical energy without the losses associated with conversion to electricity.[7]

TES systems store excess thermal energy during periods of high solar irradiance, and release the energy as required during periods of low-to-zero irradiance. Incorporating TES systems into CSP plants can address the intermittency of solar energy and enable a 24-hour supply of renewable energy. The stored energy during periods of peak production can be used to supply power during times of peak consumption, reducing or eliminating the requirement for peaker plants, which are power plants that run only when there is a high demand for electricity. [8–10] TES system can also be integrated with other methods of thermal power generation systems such as geothermal, fossil fuel, nuclear, industrial waste heat, and biomass power plants.

Despite the potential of TES systems to improve CSP, research into their implementation remains largely confined to laboratory-scale experiments.[2] Metal hydrides that can hydrogenate and dehydrogenate reversibly at high-temperature and high-pressure are considered candidate materials for TES. The thermodynamic and kinetic properties of these metal hydrides, however, are poorly defined due to the limitations of the measurement techniques at such temperature and pressure regimes. This thesis highlights a custom-designed calorimeter that operates up to at least 1232 ^{o}C and 33 bar hydrogen pressure so that the heterogeneous reactions of these metal hydrides can be studied.

1.2 Review of thermal energy storage (TES) technologies

TES is a technology that stocks excess thermal energy in a storage material over a period of time (hours, days, or even months) so that the stored thermal energy can be released later for power generation. The storage material is selected based on the cost, reactivity, and thermal and chemical stability to provide a robust system that can operate for thousands of cycles.[11] These storage materials undergo three steps during operation: charging; storage; and discharging.[2] The operating temperature of each of these steps can affect the overall efficiency and cost of the system. There are two key strategies for reducing cost and increasing total heat storage capacity: utilizing high energy density TES materials to lower the material cost; and operating the TES system at high temperature to increase the energy conversion efficiency.[12] The second strategy can be explained by the definition of heat engine efficiency. The theoretical maximum efficiency, Carnot cycle efficiency, can be expressed as:

$$\eta = 1 - \frac{T_c}{T_h}$$

where η is the overall energy conversion efficiency, T_c and T_h are the lowest and highest temperatures in an energy conversion cycle, respectively.

Based on the working principle and the storage material, TES systems can be broadly classified into three types: sensible heat storage; latent heat storage; and thermochemical storage.

Sensible heat storage utilizes materials that absorb and release heat associated with a temperature change. This storage method is described by the equation:

$$Q = mC_p\Delta T$$

where $\boldsymbol{C_p}$ is the specific heat of the material, $\boldsymbol{\Delta T}$ is the temperature change, $\boldsymbol{m}$ is the mass of the material. The predominant sensible heat storage material is a molten salt comprised of a binary salt system of 60% KNO_3 and 40% $NaNO_3$. This material has a fast charging speed that can directly be used as the heat transfer media in a CSP plant. Unfortunately, molten salt is corrosive and solidifies under 200 ^oC, which requires suitable insulation and extra energy to maintain the storage temperature. About 4% of the solar energy captured by the CSP plant is required to maintain the molten salt temperature at zero irradiance periods.[12] Moreover, a large volume of molten salt is required to store thermal energy because the typical maximum outlet temperature of the molten salt is only around 565 ^oC. In this sense, the gravimetric heat capacity for sensible heat storage is only ~0.02-0.03 kWh kg^{-1}, which is much lower than the energy density of a typical lithium-ion battery (~0.15-0.26 kWh kg^{-1}).[13]

The latent heat storage uses heat exchange during phase change, typically during the melting and solidifying process. The thermal energy storage capacity can be represented by the equation:

$$Q = mL_f$$

where $\boldsymbol{L_f}$ is the latent heat of fusion. The latent heat of fusion is known to be higher than the specific heat for most materials. For example, the ratio of latent heat of fusion to the specific heat of water is 80, while this ratio is around 120 for $NaNO_3$.[11] A much greater energy storage capacity than sensible heat alone can be achieved when combining two storage methods together. A limitation of this technology is that the operating temperature is relatively low and needs to be cycled around the melting temperature (~300-400 ^oC). Therefore, although latent heat storage method has a higher energy density than sensible heat storage, the overall energy conversion efficiency is compromised by a lower operating temperature.[2]

Compared to the two technologies mentioned above, thermochemical TES utilized reversible chemical reactions that typically have at least 5 to 10 times higher energy storage capacity.[12] (Table 1.1) The following reaction will happen during the charging and discharging process:

$$A + \Delta H_r \rightleftharpoons B + C$$

where A, B, C represent chemical species involved in the reaction and ΔH_rrepresents the enthalpy change. The forward endothermic reaction converts thermal energy into chemical energy within the storage material. During the discharging step, the energy storage material B and C react exothermically to produce A and the heat generated can be directly used to produce electricity. For example, metal hydride TES materials endothermically decompose to

metal and hydrogen gas during the charging step and the hydrogen gas can be stored separately. During the discharging step, the reaction between hydrogen gas and metal produces metal hydride and release heat that can be converted to electricity.

	Sensible heat	Latent heat	Thermochemical
Volumetric energy density	~50 kWh m^{-3}	~100 kWh m^{-3}	~500 kWh m^{-3}
Gravimetric heat storage capacity	~0.02-0.03 kWh kg^{-1}	~0.05-0.1 kWh kg^{-1}	~0.5-1 kWh kg^{-1}
Storage temperature	Charging step temperature	Charging step temperature	Ambient temperature
Storage period	Limited due to thermal loss	Limited due to thermal loss	Theoretically unlimited

Table 1.1 Summary of three TES methods. The sensible heat TES has already been employed in CSP plants, while the thermochemical TES is still at an early stage of academic research. Table adapted from Pardo *et al*., *Renewable and Sustainable Energy Reviews*, vol. 32, (**2014)**, 591:610.[2]

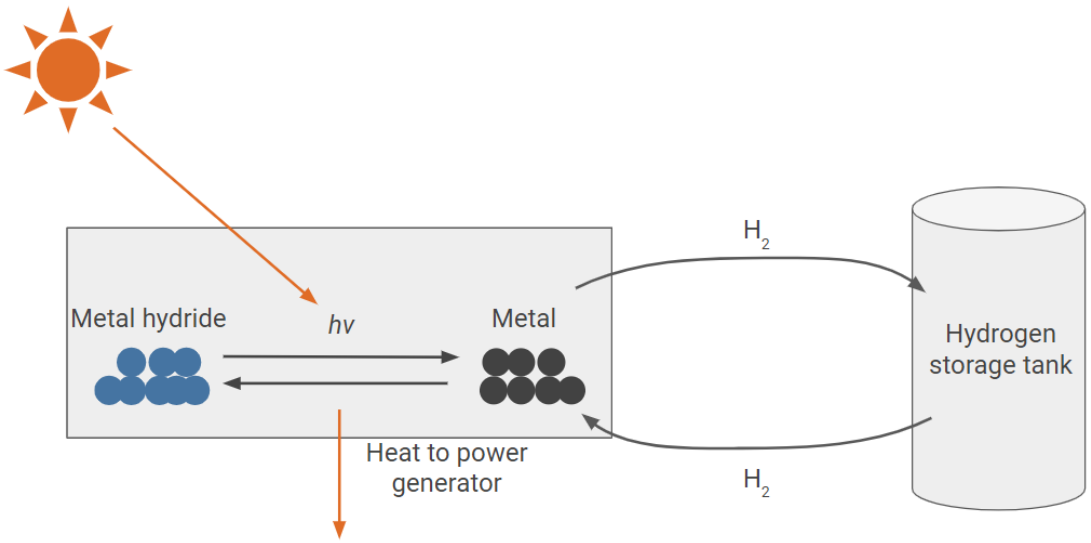

Fig. 1.1 Schematic of the working principle of the thermochemical TES system. Concentrated solar heat is collected to drive the metal hydride dissociation. The resulting hydrogen gas is separated and stored temporarily in another container. At times with weak or zero solar irradiation, hydrogen gas is released to react with metal so that the generated heat can drive the power plant.

Multiple classes of materials including metal hydrides, oxides, sulphides, carbonates, and ammonia have been studied as candidates in thermochemical TES.[12] One of the major advantages of thermochemical TES over sensible heat storage and latent heat storage is that the materials can be stored at ambient temperature and thus the energy can be stored for a sufficiently long period.[2] This feature is significant because it makes the transportation of energy storage media possible and makes the CSP plants dispatchable. Thermochemical TES materials research, however, is still in its infancy and further thermodynamic data at high temperatures and pressures are still required to aid the design of high efficiency and low cost TES systems.[14]

1.3 Thermochemical TES materials

There are a number of thermochemical TES materials that operate at a high temperature and can potentially be used to increase the overall energy conversion efficiency. These materials must have the following characteristics: enable reversible reactions without by-products; have energy densities > 500 kWh m^{-3}; enable faster reaction kinetics than the rate of heat transport (to quickly store and release energy with minimum energetic losses); have decomposition temperatures of < 1000 ^{o}C; and have recombination temperatures of > 500 ^{o}C.[2,15,16] Materials that can satisfy these criteria include a number of metal oxides, metal carbides, and metal hydrides. Among these classes of compounds, metal hydrides such as MgH_2 and LiH offer the highest energy density at the same operating temperature level. (Fig. 1.2)

The most widely studied metal hydride system for application in thermochemical TES is MgH_2 due to its high gravimetric hydrogen storage capacity (7.7 wt%), relatively low cost, and high abundance.[2,14,16,17] The use of MgH_2 itself for TES, however, is impractical because of the slow reaction kinetics and high thermodynamic stability of its hydride. The formation of MgH_2 takes hours even at 400 ^{o}C and 10 bars of H_2 pressure.[18,19] The derivative compounds of MgH_2 have been shown to reversibly decompose and recombine with cycle times on the order of 3 hours, with Mg_2NiH_4 exhibiting a hydrogen storage capacity of ~3 wt% over the course of > 1000 cycles at temperatures of 230-330 ^{o}C and hydrogen pressures of 0.4-4 bar,[20] and Mg_2FeH_6 exhibiting a hydrogen capacity of 5 wt% over the course of >500 cycles at temperatures of 480-533 ^{o}C and hydrogen pressures of 80-86 bar.[21] (Table 1.2) The reaction mechanisms and cyclability of these compounds at a temperature higher than 600 ^{o}C has yet to be studied, which is necessary for a high efficiency TES system.

Chemical System	Operating temperature and pressure (K)	Operating pressure (bar)	Hydrogen capacity (wt %)	Cyclability
MgH_2	623 - 773	40 - 130	7.66	~ 700
Mg_2NiH_4	523 - 623	0.4 - 4	3	> 1000
Mg_2FeH_6	753 - 806	80 - 86	5	> 500

Table 1.2 Several Mg-based metal hydrides that are tested and reported from the literature.

An alternative metal hydride system for use in TES systems is LiH, which is attractive due in part to its high theoretical gravimetric heat storage capacity (~8300 kJ kg^{-1}) compared to that of MgH_2 (~2800 kJ kg^{-1}).[14] The high decomposition temperature of LiH (> 1000 ºC) precludes it from use as a fuel for TES. This temperature, however, is decreased to ~567 ºC in the presence of aluminum, and both the decomposition and reformation reactions are reversible.[22] The decomposition temperature of LiH has also been observed to be reduced in mixtures of LiH with Si, Ge, and Sn.[23–25] More recently, Sheppard and coworkers prepared a homogenous 1:1 mixture of Al and LiH using ball milling and analyzed the hydrogen adsorption and desorption pressure composition isotherms at a number of temperatures using a Sievert's apparatus.[26] The operating temperature of the system (at H_2 pressure of 1 bar above the sample) was observed to be 574 ºC and the kinetics of the system sufficiently fast for equilibrium to be reached within 2 hours. Moreover, the theoretical energy density of the system (~1400 kJ kg^{-1}) was found to be comparable to Mg_2FeH_6 (~2100 kJ kg^{-1}).[27]

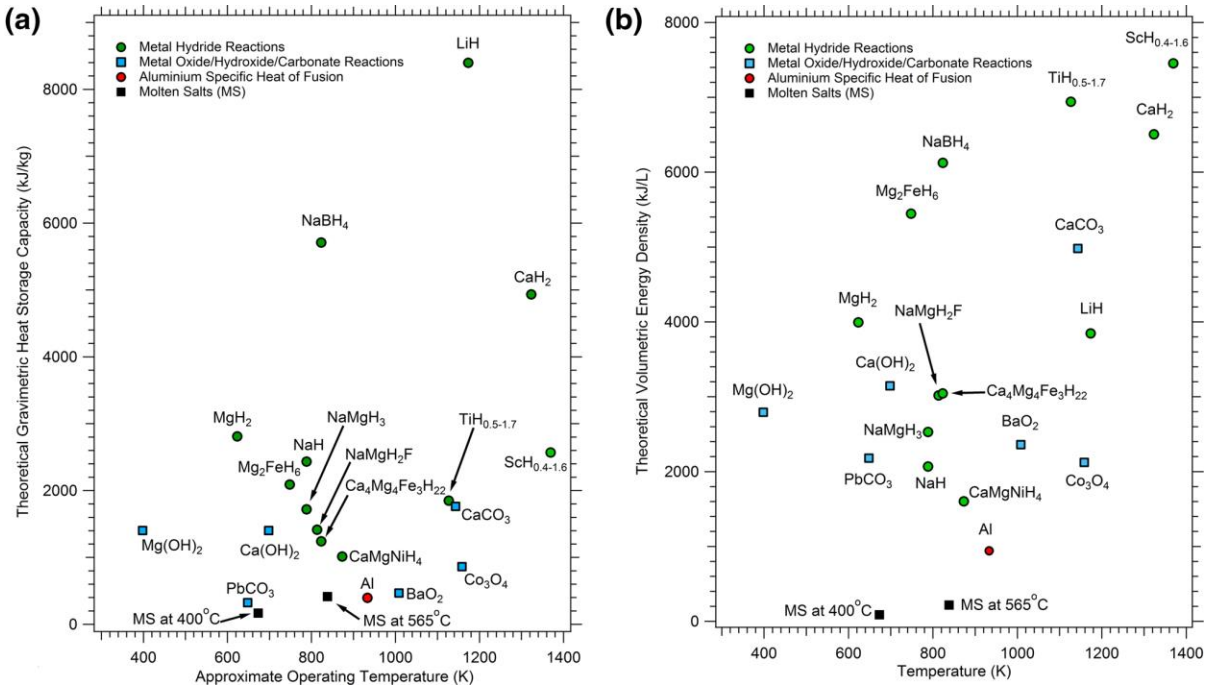

Fig. 1.2 Theoretical gravimetric heat storage capacity (a) and theoretical volumetric energy density (b) and approximate operating temperatures of metal hydrides, metal oxides/ hydroxides/carbonates, aluminum latent heat of fusion and metal salts. Note that a few metal hydrides have high energy density and have a high operating temperature (> 1000 K) which is the condition with higher operating efficiency. Figure adapted from Sheppard et al., Appl. Phys. A, (2016), 122:395.14

Alkali and alkaline earth metal hydride systems (including MgH_2 and LiH) can provide an energy storage density 20× higher than a molten salt TES and 5× higher than a metal oxide and ammonia thermochemical TES.[12] One possible reason that theses alkali and alkaline earth metal hydrides are not well studied at high temperatures (~ 900 - 1100 K) is that many of these metal hydrides have their reversible decomposition-regeneration temperature that falls outside of the temperature range of current thermal analysis technologies (typically < 800 - 900 K). They are also not been well-studied for thermochemical TES in terms of kinetic information and long-term stability over cycling. Therefore, we can build a custom-designed calorimeter

to study high-enthalpy hydrides of the alkali and alkaline earth metals at high temperatures and high pressures.

Chemical System	Operating temperature and pressure	Hydrogen capacity (wt %)	Gravimetric energy density (kJ/kg)	ΔH^0 (kJ/mol)
MgH_2	623 - 773 K 40 - 130 bar	7.66	2814	-75
LiH	1273 K	12.7	8397	-91
TiH_{2-x}	923 - 1025 K 1 - 10 bar	4.0	3190	-150
CaH_2	1400 - 1673 K 1 - 5 bar	4.8	4426	-186

Table 1.3 Theoretical hydrogen and energy densities for various metal hydride systems operating in high temperature and pressure regimes.

1.4 Calorimetry technologies

Currently, two types of thermal analysis technologies including thermogravimetric analysis (TGA) and differential scanning calorimetry (DSC) are used in the thermochemical TES material study. TGA is a method for measuring mass change of a sample under temperatures and gaseous atmospheres of interest. A 1 μg resolution scale affixed inside a high-temperature furnace is used to resolve the mass gains or losses resulting from a chemical reaction or phase changes at temperatures as high as 2000 °C.[28] Since the TGA experiment is carried out in an environment with gas flux rather than a closed chamber, the gas-solid phase equilibrium related to pressure change cannot be observed.[29]

A differential scanning calorimeter (DSC) is an instrument that determines the heat absorbed or released by a sample. It is used to measure specific heat, latent heat of phase change, and reaction enthalpies. Zuttel and coworkers designed and constructed a high-temperature and high-pressure DSC which can operate at 600 °C and 200 bar to investigate hydrogenation and dehydrogenation of hydrides *in situ*.[30] The upper bound of the temperature is limited at 600 °C because one of the alloys in the reaction chamber (Incusil-ABA) has the melting range between 605 - 715 °C.

Therefore, to study the thermal chemical material such as MgH_2 and LiH at high-temperature and high-pressure, a customized calorimeter needs to be designed and a thermal analysis algorithm needs to be developed. This thesis reports a novel calorimeter designed and constructed by my colleagues and I in the Berlinguette research group. The physical design of the calorimeter and a finite element analysis (FEA) model are highlighted in Chapter 2. The calorimeter is demonstrated at working temperatures from 1232 °C while under pure hydrogen pressures up to 33 bar. The FEA model is validated by comparing the data from the calibration experiment and the COMSOL model simulation.

Chapter 3 highlights a two-state lumped element model that is developed to calculate the enthalpy of the chemicals based on the temperature data from the calorimeter. A non-linear regression method is used to fit the data and to estimate the heat transfer parameters in the model. This model was demonstrated using an aluminum heat of fusion measuring experiment, as well as exothermic process simulation and obtained a fitting accuracy of over 99%.

Chapter 2: High temperature and pressure calorimeter design

Part of this chapter is published in the paper MacLeod *et al*., *Review of Scientific Instruments*, **88**, 084101 (2017)[1] Ben MacLeod, Brian Lam and I were responsible for the physical design using CAD software and fabrication of the calorimeter including the heater coil, pressure vessel, isothermal cooling jacket, thermocouple positioning. Phil was responsible for the design of the control software by LabVIEW. I am also responsible for building the finite element analysis model using COMSOL.

2.1 Introduction

The study of thermochemical energy storage materials operating above 500 °C is motivated by the increased Carnot efficiency that can be achieved by operating concentrating solar power plants at elevated temperatures.[2] Metal hydrides exhibit reversible, endothermic dehydrogenation reactions appropriate for TES[14,31] and numerous metal hydrides decompose in the 500-1150 °C temperature range.[14] Several metal hydrides require high pressures of hydrogen to drive the exothermic rehydrogenation necessary to recover the stored thermal energy, as shown by the dissociation pressure curves in Fig. 2.1.

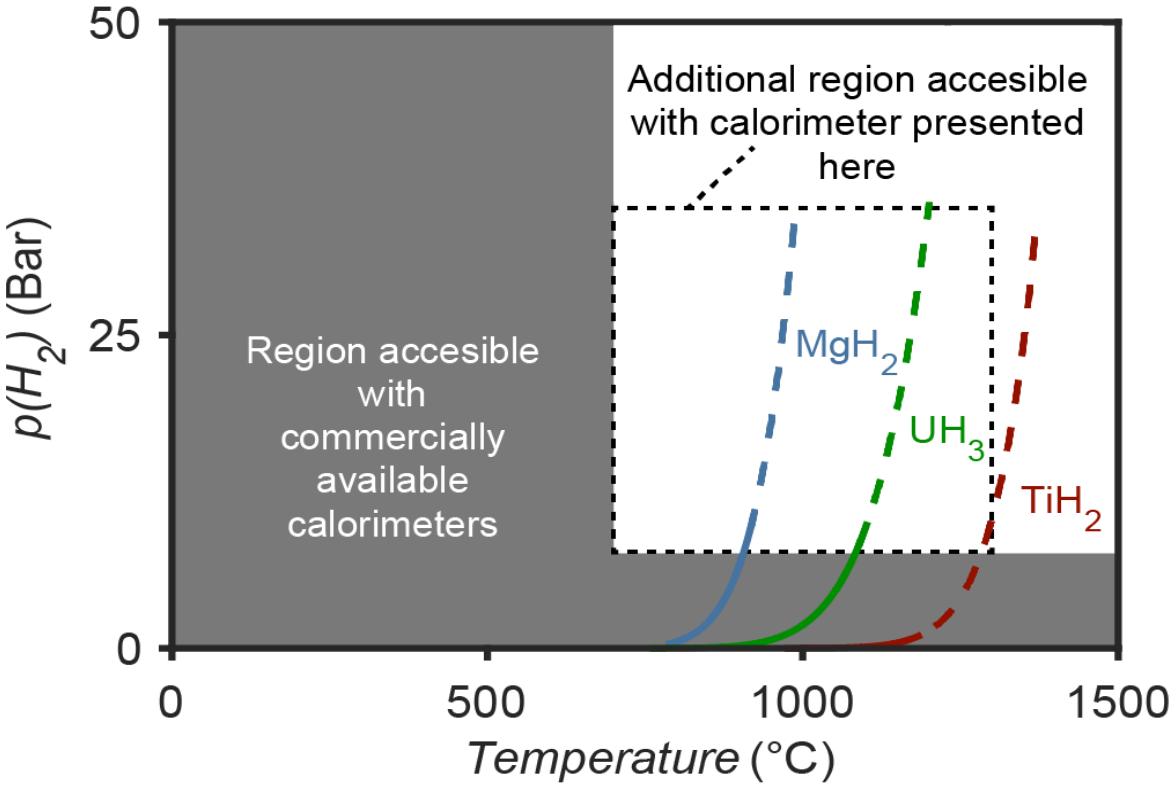

Fig. 2.1 Range of operation for commercially available calorimeters (grey shaded region; see supplementary Table S1 for details) and for the instrument reported here that enables calorimetric studies in a previously inaccessible temperature and hydrogen pressure regime. Decomposition pressure-temperature curves for selected metal hydride systems are indicated; the solid parts of the curves are data extracted from Sandrock's review of hydrogen storage materials,[4] and the dashed parts of the curves are extrapolations from that data according to the Van't Hoff equation. (Reproduced from MacLeod *et al*., *Review of Scientific Instruments* **88**, 084101 (2017), with the permission of AIP Publishing)

By resolving solid-solid and solid-liquid phase changes in addition to kinetic and thermodynamic data for heterogeneous reactions, variable-pressure calorimetric measurements can provide richer data for the study of candidate TES reactions than the more commonly employed thermogravimetric measurements. For example, a study employing simultaneous calorimetry and thermogravimetry found an irreversible solid-state transition between polymorphs of $Mg(BH_4)_2$ at 200 °C that could be detected via calorimetry but

produced no TGA signal.[32] In that study, calorimetry also provided information about decomposition reaction steps that were not clearly evident from the gravimetric data alone.

Constructing calorimeters that operate at high temperatures and high hydrogen pressures poses numerous engineering challenges. Few materials are available that retain strength, pressure integrity, and chemical inertness under these extreme conditions. Heater elements and temperature sensors are subject to chemical attack at high temperatures, particularly by reactive gases such as hydrogen. Specialized calorimetric instruments operating either under high hydrogen pressures (>50 bar) at moderate temperatures (up to 700 °C) or at high temperatures (up to 1800 °C) under moderate hydrogen pressure (<10 bar) are commercially available; however, commercial instruments that operate at both high hydrogen pressures and high temperatures simultaneously are not widely available (Fig. 2.1; Table S1). All pressures quoted here are gauge pressures. The only calorimeter apparently available for studying metal hydride materials at high pressures and temperatures is a bespoke instrument that operates at hydrogen pressures up to 200 bar and temperatures up to 600 °C.[30] Here, we present an alternative calorimeter design that enables the study of gram-scale heterogeneous chemical reactions at temperatures up to at least 1232 °C while under pure hydrogen pressures up to 33 bar. The architecture of this calorimeter enables simultaneous calorimetric and pressure measurements. This instrument can provide thermodynamic, kinetic and material stability data from a single experiment, thereby facilitating the rapid experimental screening of metal hydride materials for thermochemical energy storage applications over an otherwise inaccessible range of operating temperatures and pressures.

2.2 Calorimeter design objectives

To enable studies on the widest possible range of TES materials, we built an instrument that operates over broad temperature and pressure ranges, can accommodate several milliliters of sample material, and can measure pressure changes due to gas evolution/sorption with adequate resolution to track the extent of a reaction. The chosen design objectives are outlined in Table 2.1 and our rationale is detailed further in Appendix A.

Quantity	Design objective
Maximum operating temperature	1300 °C
Maximum operating pressure	50 bar
Sample mass	>1 gram
Sample volume	10 mL
Calorimetric resolution	<100 mW
Calorimetric accuracy	<10%
Pressure measurement resolution	0.02 bar

Table 2.1 Quantitative design objectives for the calorimeter chosen to enable a wide range of studies on metal hydride TES materials. (Reproduced from MacLeod *et al*., *Review of Scientific Instruments* **88**, 084101 (2017), with the permission of AIP Publishing)

2.3 Design details

Our concept for avoiding degradation of the calorimeter heater and temperature sensors is to confine the sample solids and gases within a chemically inert, pressurized reaction tube while placing the heater and sensors outside the tube. A tubular geometry is practical for such a pressure vessel because high purity alumina ceramic tubes which retain

high strength and chemical inertness at high temperatures are readily available. As a basis for our design, we selected an alumina tube (Coorstek AD-998) with a 0.5" outer diameter and 0.375" inner diameter. We predict this tube will rupture at 221 bar internal pressure when the tube is at 1300 °C (see Appendix C), but we did not test the system at hydrogen pressures greater than 33 bar.

Our calorimeter design is illustrated in Fig. 2.2 The sample and reaction tube are heated by a heater consisting of a 6" long, 0.55" ID helix of resistive wire (Sandvik Kanthal A-1). At either end of the helix, this heater terminates in a straight section of wire which extends axially out of the isothermal jacket and connects to a power cable. To reduce the required heater input power, the heater is surrounded by a 1.5" ID × 9" OD × 12.5" long insulating cylinder consisting of a stack of ten insulating firebricks (Morgan Thermal Ceramics K26) cut into semi-annuli with an abrasive waterjet. This cylinder is held together by a modular liquid-cooled isothermal copper jacket. The 1.5" diameter cavity within the cylinder allows the heater to radiate freely in all directions, minimizing the possibility of heater failure due to localized overheating.

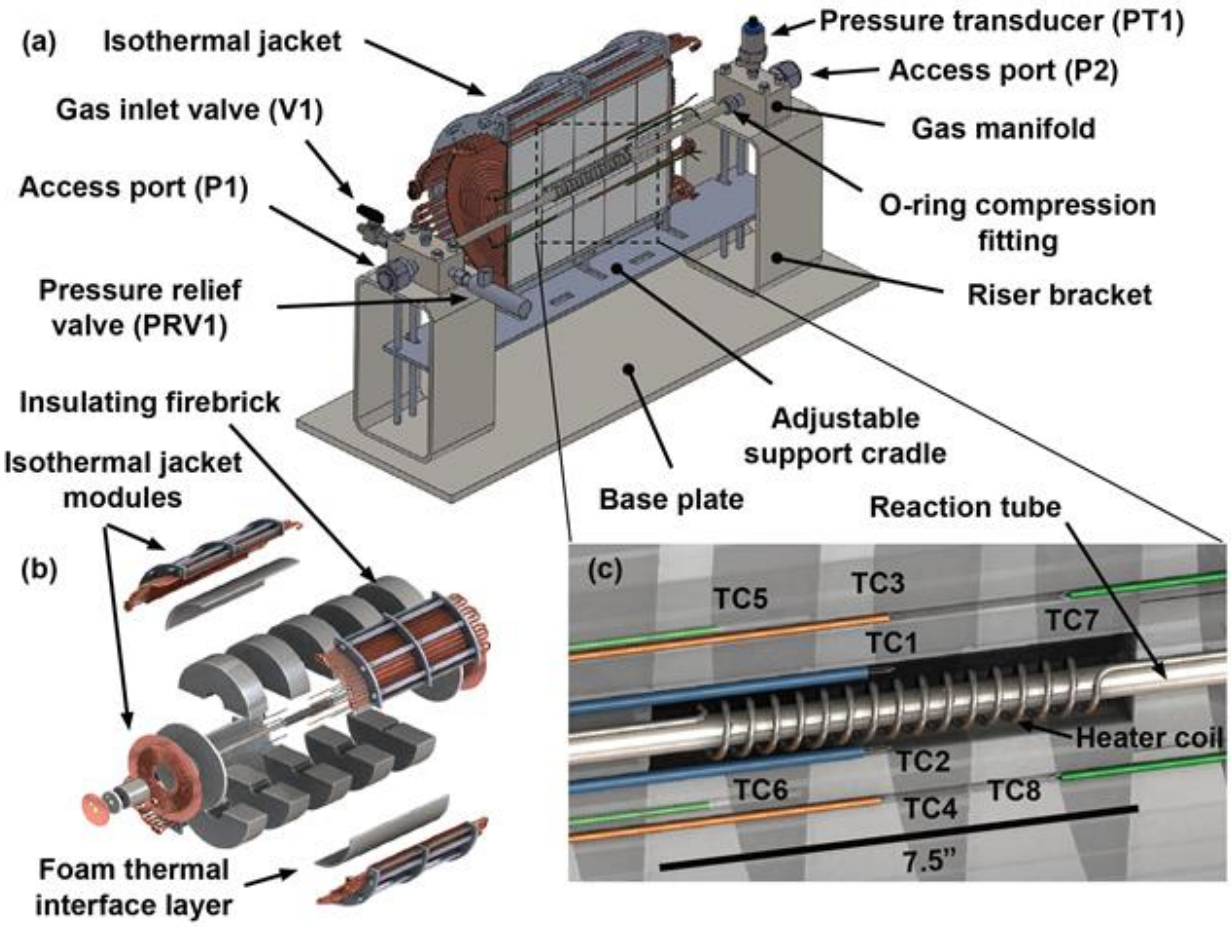

Fig. 2.2 Mechanical design of the calorimeter. (a) Overview of the instrument with one half of the isothermal jacket and furnace insulation cut away. (b) Exploded view of the furnace, showing the ten insulating fire bricks and the surrounding modular isothermal jacket consisting of four quadrants, two end plates and corresponding elastic foam thermal interface layers (c) Detail view of the hot zone showing the locations of the heater and the eight internal thermocouples (orange, green and blue cylinders, TC1 - TC8). Not shown are six additional thermocouples epoxied to the isothermal jacket (TC9 - TC14), one on each quadrant and each endplate. (Reproduced from MacLeod *et al*., *Review of Scientific Instruments* **88**, 084101 (2017), with the permission of AIP Publishing)

As shown in Fig. 2.2 (c), an array of thermocouples samples both the radial and axial temperature gradients around the furnace hot zone. The two thermocouples closest to the heater (TC1-2) are 24 AWG R and S-type precious-metal thermocouples rated to 1480 °C

(Reotemp Inc.) More economical 24 AWG N-type thermocouples rated to 980 °C (Reotemp Inc.) are anchored into the firebrick at six locations about the hot-zone (TC3-8) using ceramic putty (Cotronics 7020). Six additional 24 AWG N-type thermocouples are mounted on the isothermal copper jacket, one on each face of the cylinder and four evenly spaced around the circumference, approximately halfway along the length of the cylinder.

Fig. 3 provides a fluidic diagram of the instrument. To contain the sample gases, the reaction tube is sealed at each end to a hydrogen-tolerant 316 stainless steel manifold. To facilitate reaction tube exchange, this seal is made by demountable compression fittings (Swagelok Ultra-Torr™) with hydrogen-compatible 70D Viton™ O-rings. On each manifold, a copper-gasketed, 0.75" VCR fitting (Swagelok) provides an access port enabling easy, axial exchange of both sample crucibles and reaction tubes. One manifold provides connections for charging gases into and venting gases from the reaction tube via two ball valves (Swagelok SS-42GVCR4) and an adjustable pressure relief valve (Swagelok SS-4R3A1). A pressure transducer (Endress+Hauser Cerabar PMC131) is mounted on the other manifold. This pressure transducer was selected because it has a ceramic diaphragm compatible with reactive gases including hydrogen.

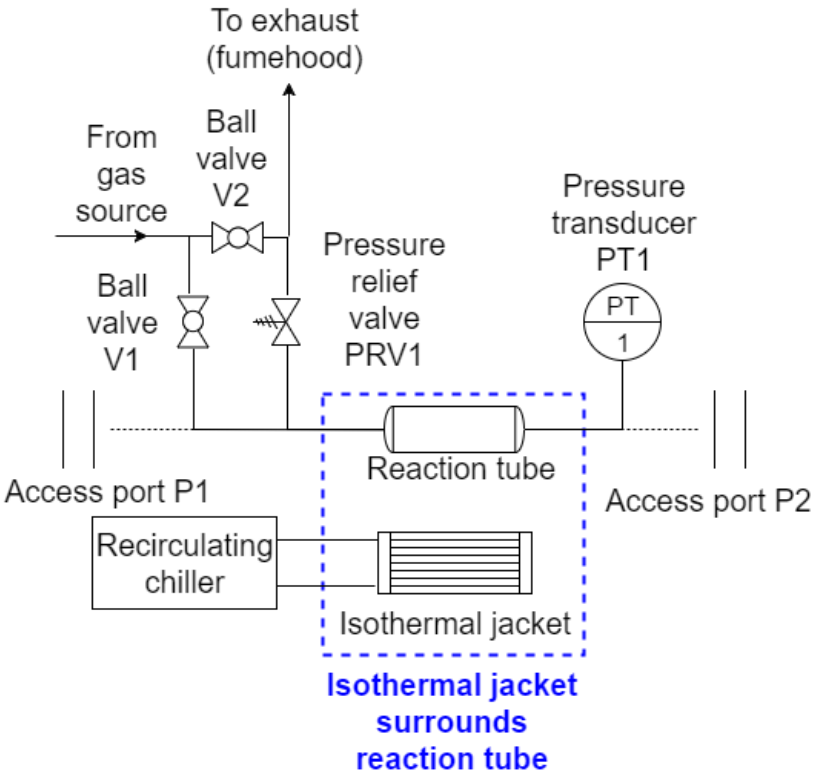

Fig. 2.3 Instrument fluidic diagram. Capped VCR flanges on either end of the reaction tube (P1, P2) provide access for sample and reaction tube exchange. Gases may be introduced into the reaction tube from a gas source via valve V1. PRV1 protects the system against overpressure events, while V1 and V2 can be used to manually vent the system. V1 enables the reaction tube to be isolated from the gas distribution network during experiments. PT1 provides continuous measurements of the pressure in the reaction tube. The temperature of the isothermal jacket is regulated by a recirculating chiller. (Reproduced from MacLeod *et al.*, *Review of Scientific Instruments* **88**, 084101 (2017), with the permission of AIP Publishing)

The modular isothermal jacket consists of four quadrants and two end plates fabricated from copper sheets and tubes. This jacket compresses the insulating brick cylinder via a silicone foam elastic thermal interface layer (Rogers BF2000). The temperature of the jacket is regulated to approximately ±3°C by running coolant through the six jacket modules in parallel. A recirculating chiller (Koolance EXC-800) provides coolant at a temperature regulated by an onboard on-off controller and a thermocouple positioned on the jacket

surface. This configuration provides an approximately isothermal boundary condition in order to simplify heat transfer modelling. An adjustable aluminum cradle supports the entire furnace assembly and facilitates alignment of the furnace to the reaction tube.

The instrument operates using custom software built using National Instruments LabVIEW, which interfaces with several National Instruments data acquisition modules and the furnace power supply. The furnace power supply is a 720 W DC programmable supply (Keithley 2260B-30-72) that provides power to the ~0.3-ohm heater coil. A DC supply was selected because sufficiently precise AC power supplies were found to be too costly for this application. Thermocouple and transducer outputs are sampled at 1 Hz.

Samples are loaded into the calorimeter inside 0.25" OD x 0.188" ID x 4" long tubular alumina crucibles that provide sufficient volume to contain gram-scale quantities of sample material. Once sample powders have been introduced into the crucible, the circular ends of the cylindrical alumina crucible are sealed with refractory putty to contain the sample. A series of holes in the crucible wall enable gas exchange between the sample and reaction tube gas space. Alumina rods of a calibrated, pre-measured length is utilized to accurately center crucibles within the hot zone of the instrument.

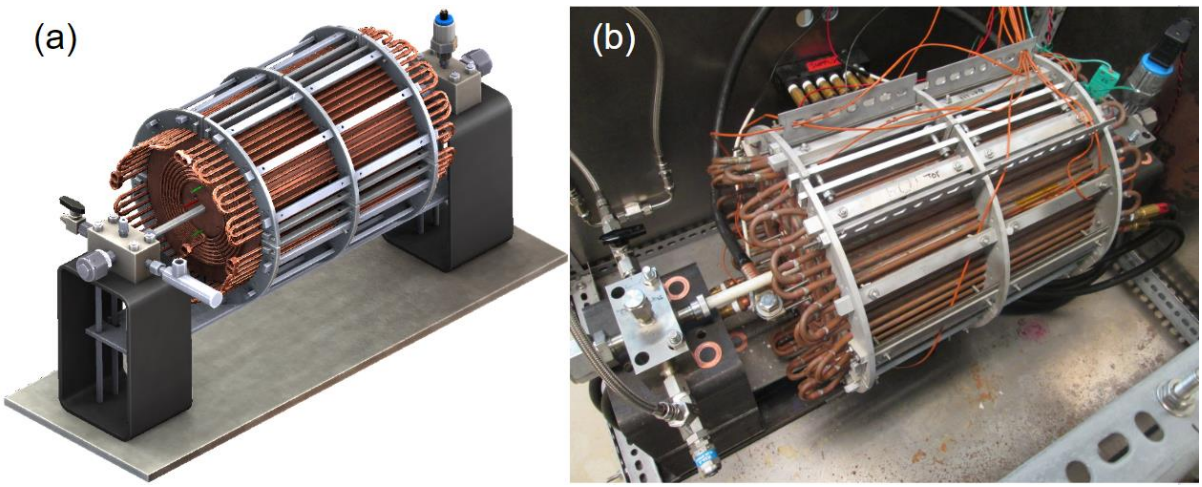

Fig.2.4 The calorimeter CAD overview by Solidworks (a) and the calorimeter after built (b). The calorimeter is anchored in a steel blust box which is designed to prevent damage in the event of hydrogen gas explosion.

2.4 Finite element analysis (FEA) model using COMSOL Multiphysics®

A COMSOL Multiphysics® finite element analysis (FEA) model has been built to simulate the relationship between the input power and the temperature profile at different positions in the calorimeter. This model can help us understand whether the calorimeter can achieve the required temperature with certain input power and predict the temperature profile as a function of time to aid experimental design.

A simplified 2D axisymmetric model has been employed in COMSOL to represent the cylindrical geometry of the instrument body. (Fig.2.5) The heating coil is simplified and represented by identical rings uniformly distributed along the reaction tube in the heating zone. The long rectangular near the center axis represents the reaction tube and the bulk rectangular block represents the cylindrical body of the calorimeter. Four temperature probes were placed in the 2D model as shown in Fig.2.5 and they represent the thermocouple positioning in the actual instrument. The model is based on this 2D plot revolving around the

central axis to form a 3D plot. The 2D axisymmetric methodology requires far less computational power relative to a 3D model, rendering it particularly convenient for a cylindrical instrument.

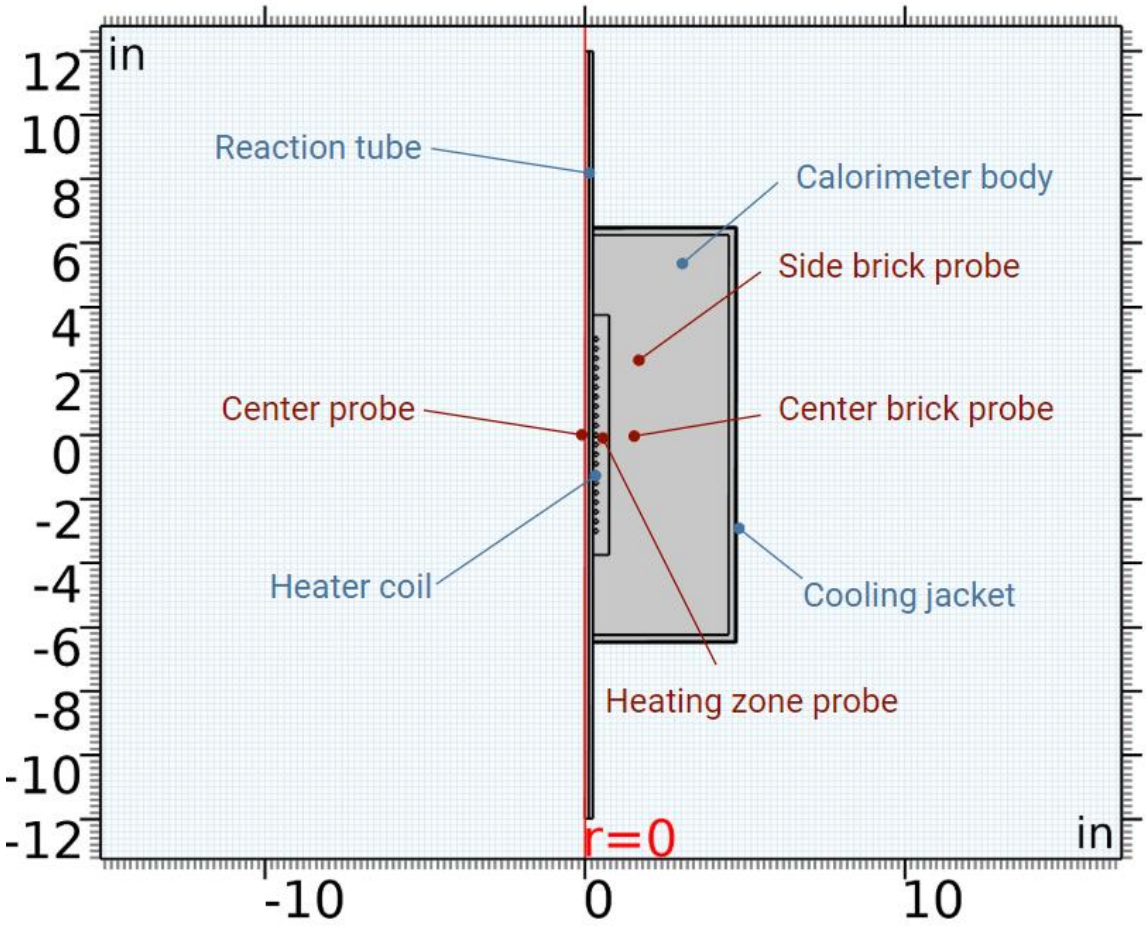

Fig. 2.5 A 2D axisymmetric model plot by COMSOL. The long rectangle represents the reaction tube and the bulk rectangle represents the calorimeter body. The heater coil is represented by the small circles in the middle of the plot, which is revolved around the center axis to form the rings. The four labelled dots are the position of virtual probes that have the same location of the thermocouples (TC1, TC2 in the heating zone.TC3, TC4 in the brick on the center horizontal line. TC5-8 in the 2.5" above below or above the center horizontal line)

In practice, a portion of the heater coil is not positioned within the heating zone but is either buried in the bricks or leading to the power connections that are located outside of the instrument. A calculation showed that around 70% of the length of the heating coil is located in the heating zone. Therefore, in the simulation, all the input power was reduced to 70% of its original value. The material properties that have been used in this model are supplied directly by the vendor or interpolated from the material datasheet. Since the outer cooling jacket was cooled by a chiller, the temperature of the outer surface of the instrument body was set at a constant 15 ^{o}C. The initial temperature of the other parts except the cooling jacket was set to be room temperature, 25 ^{o}C. All the corners and edges and the ends of the reaction tube were assumed to be thermally insulating to simplify the model.

A 0 to 1000 W power input sweep was carried out to study the instrument temperature at steady state. The results of the simulation showed that at equilibrium, a 350 W input power (before correction) was able to heat the inner heating zone to 1281.8 °C. (Fig. 2.6, Fig 2.7) It also showed that the temperature of the center of the reaction tube was 1295.2 °C.

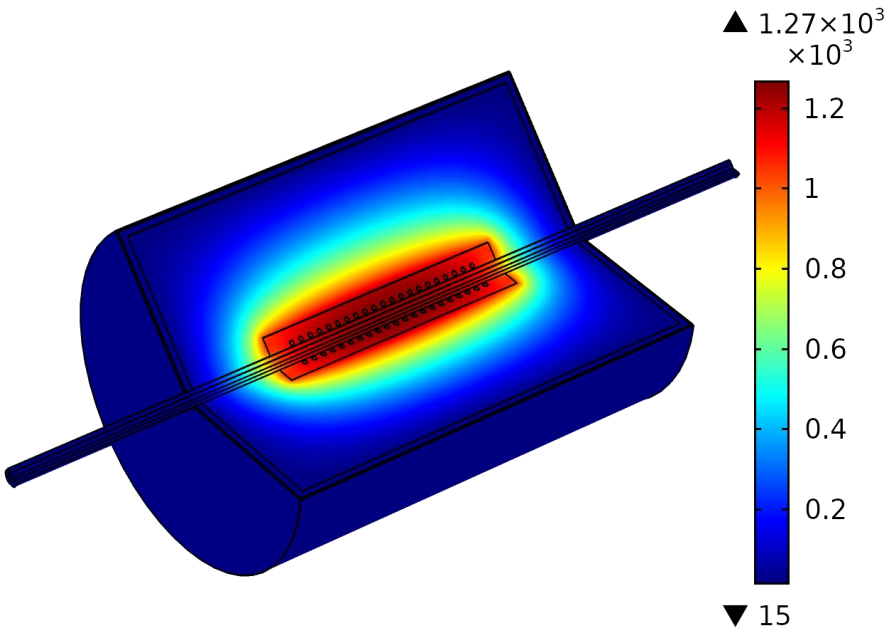

Fig. 2.6 Temperature distribution of the calorimeter at equilibrium with 350 W heater input power. The temperature of the outer surface of the cooling jacket is fixed at 15 °C.

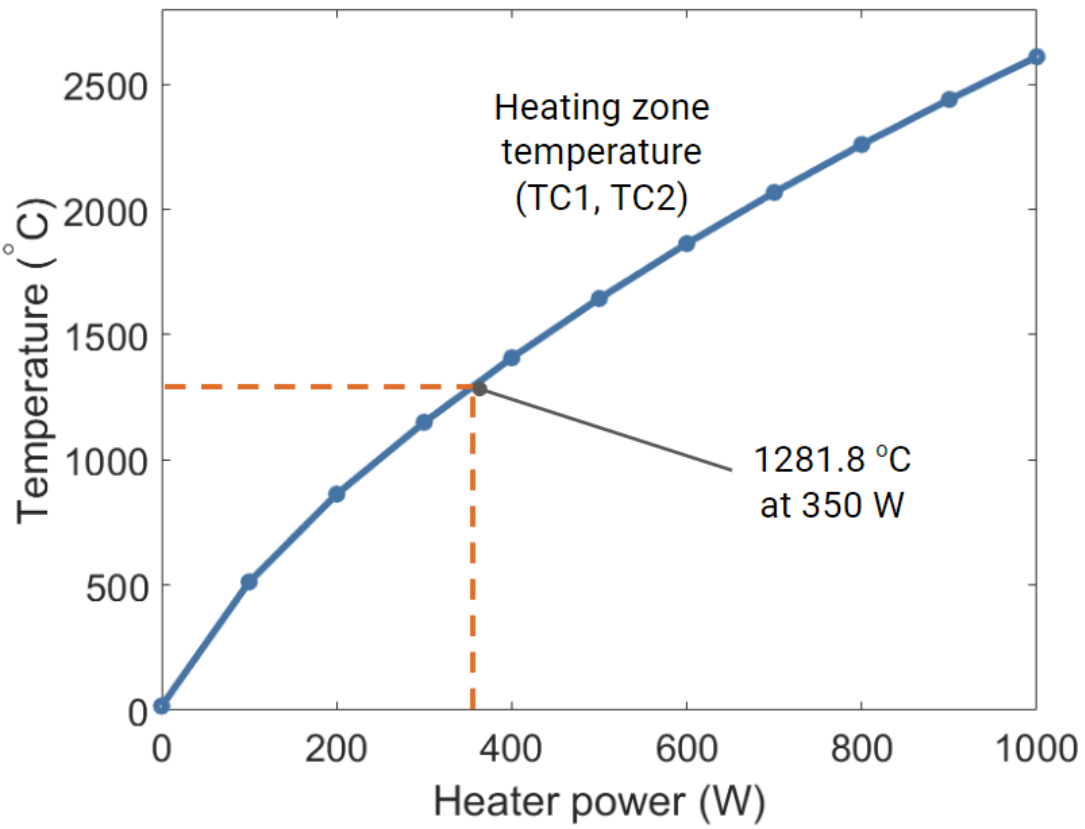

Fig. 2.7 The steady-state heating zone temperature with different heater powers. The model predicts that 350 W power is able to heat the heating zone to 1281.8 °C. Note that all the input powers were scaled to 70% of their original value due to the simplification of the geometry of the instrument.

2.5 Experimental demonstration and FEA model verification

The mechanical integrity of the instrument at high temperature and the pressure was demonstrated by charging the reaction tube with 27 bar of hydrogen while the entire apparatus was at ambient temperature and then stepping the heater power in 3 stages from 0 W up to 350 W with 150 min heating time for each stage. The highest measured temperature (at TC1) was 1232 °C. Due to the thermal expansion of the gas, the pressure reached a maximum of 33 bar. The temperature and pressure data recorded during the experiment are

shown in Fig. 2.8. Because only a portion of the gas in the reaction tube is at elevated temperature, the pressure rise due to thermal expansion of the gas is much less than if the entire volume of gas were elevated to the sample temperature. The ratio of maximum pressure to initial pressure suggests that the average temperature of the gas increased by a factor of $33\ bar/27\ bar = 1.22$ or from 25 °C to around 90 °C. Based on the internal volume of 95 mL as estimated from the CAD model, and a temperature-corrected pressure decrease of 0.575 bar over the course of the experiment, we estimate an average hydrogen leak rate of 2.28 $mL \cdot bar \cdot hr^{-1}$ over the course of the experiment. The noise on the raw pressure data is of amplitude 0.005 bar.

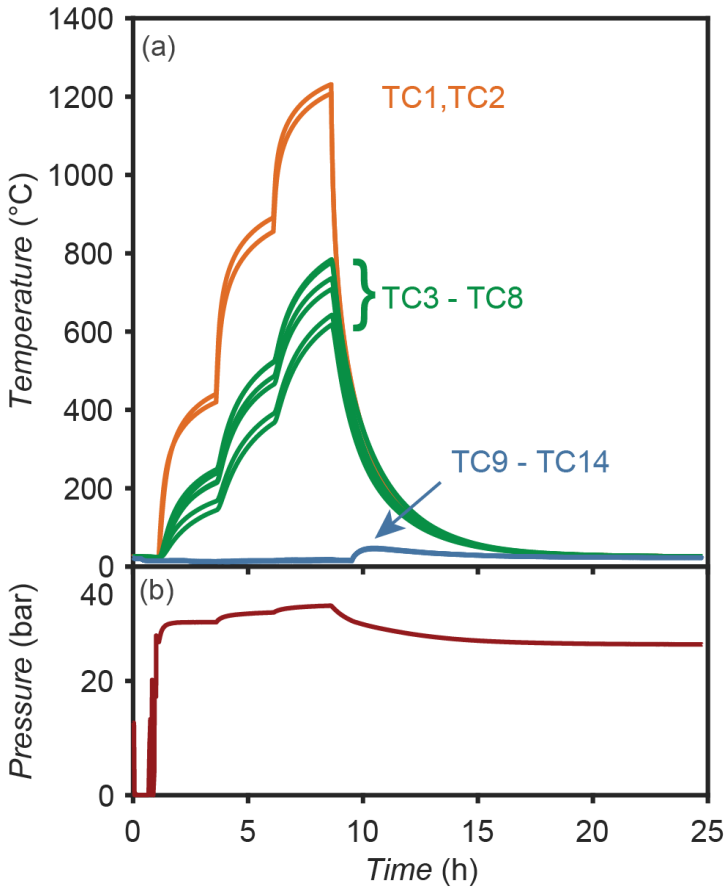

Fig. 2.8 Raw temperature (panel a) and pressure (panel b) data demonstrating operation at 33 bar and 1232 °C. The fourteen thermocouple temperatures are indicated in three groups (orange, green and blue traces) because our model-based data analysis procedure makes use of only three averages of the measured temperatures, T_a, T_b and T_s. T_a is the average of thermocouples TC1 and TC2, T_b is the average of thermocouples TC3-TC8, and T_s is the average of the six thermocouples on the isothermal jacket (see section V). The chiller was turned off shortly after the main heater power steps down to 0 W, hence the rise in the cooling jacket temperatures (TC9-TC15) shortly before time = 10 h. The isothermal jacket temperature stability is approximately ±3 °C while the chiller and furnace are running. (Reproduced from MacLeod *et al*., *Review of Scientific Instruments* **88**, 084101 (2017), with the permission of AIP Publishing)

A COMSOL simulation with the same three-step power input conditions has been carried out. In each stage, the powers were all corrected to 70% of their nominal values. A 500 min cooling period was also applied in the model to simulate the cooling time required to reach room temperature again. The result of the simulation together with the calibration experimental data has been plotted in Fig. 2.9. Note that the average temperature has been calculated for different thermocouples in the same or mirrored positions. Therefore, only three lines have been shown to represent the temperature at different positions. The R^2 goodness-of-fit was used to estimate the fitting accuracy by comparing experimental temperature profile and the simulated temperature. The R^2 goodness-of-fit is defined in the following equation:

$$R^2 = 1 - \frac{\sum_{t=1}^{N}(T_{i,measured}(t) - T_{i,simulated}(t))^2}{\sum_{t=1}^{N}(T_{i,measured}(t) - \overline{T}_i)^2}$$

The results from COMSOL simulation clearly match well with the calibration data at all positions despite a minor shift in the heating zone that is closest to the heating coil. (Fig. 2.9)

The accuracy of the fitting at three probe positions is 99.66%, 99.77% and 99.84%, respectively.

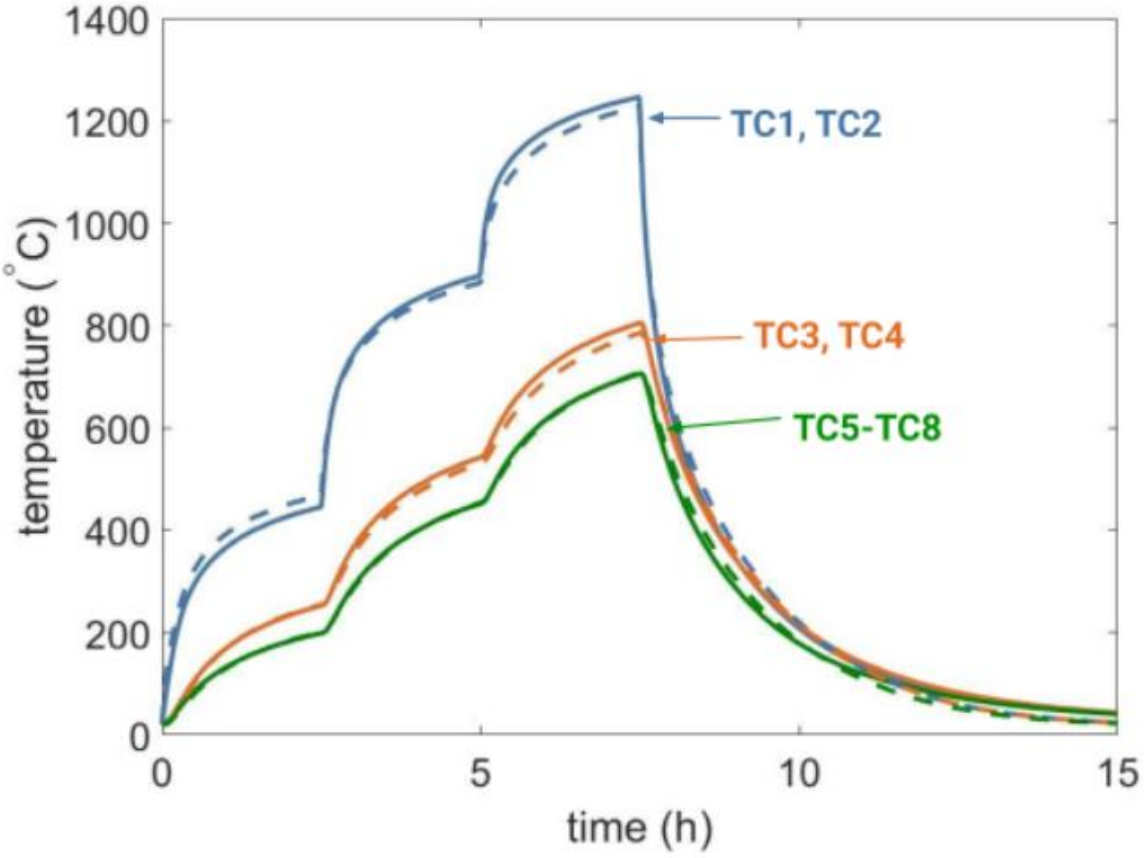

Fig. 2.9 Average raw temperature data (solid lines) and the simulated temperature profile using COMSOL FEA model (dashed lines) at three different positions (TC1 and TC2, TC3 and TC4, TC5-TC8). The accuracy of the fitted curves is 99.66%, 99.77% and 99.84%, respectively.

2.6 Conclusion

This chapter has presented an instrument for measuring heat transfer and pressure changes resulting from high-temperature reactions between gram-scale samples and high-pressure reactive gases. Operation of the instrument at 1232 °C under 33 bars of pure H_2, with a low leak-rate of 2.28 ml bars h^{-1} and pressure measurement resolution of 0.005 bars,

has been demonstrated. One key advantage of our instrument is that the temperature sensors and furnace heater elements are separated from the reactive gas space, enabling experiments with reactive gases to be carried out routinely without chemical degradation of the furnace or temperature sensors. A finite element analysis (FEA) model of the instrument was built using COMSOL and it could be used to simulate the instrument temperature responses with accuracy over 99%. Furthermore, the FEA model can predict the temperature profile as a function of time to aid experimental design. To interpret the data obtained from the calorimeter and calculate the enthalpy change of the chemicals, a non-linear lumped element model is developed and is demonstrated in Chapter 3.

Chapter 3: Thermal Analysis with a Nonlinear Lumped Element Model

Part of this chapter is published in the paper MacLeod *et al*., *Review of Scientific Instruments*, **88**, 084101 (2017)[1] Ben MacLeod and I fabricated the calibration heater, and I also collected data for the validation experiments.

3.1 Introduction

The calorimetric measurements presented in Chapter 2 requires a dynamic heat transfer model of the instrument to infer the sample enthalpy through the data of input power and output temperatures. The power of the sample and the enthalpy in a system can be calculated when relevant parameters such as the thermodynamic properties of the materials and the temperature gradient are all known and the geometry is simple. An example system is a semi-infinite thermally conductive wall with a known temperature-independent thermal conductivity that is uniformly heated on one side and maintains a constant temperature on the other side. The input power can be calculated directly from heat transfer equations when the system is assumed to be adiabatic and at steady state. This type of system is always referred to as a "white box". In our calorimeter, however, the heat transfer parameters are not initially clear due to the complex geometry and various temperature-dependent material properties. We can combine the data obtained from the calorimeter with partial knowledge of the instrument to build up a "grey box" heat transfer model that is more flexible compared to the "white box" model. Instead of obtaining heat transfer parameters of the instrument from the datasheet, the parameters are estimated by fitting the calibration temperature data with the

model. The advantage of this methodology is that it grants more freedom to the geometric configuration, samples and sensors, while the greatest challenge is to develop a heat transfer model as close to reality as possible.

3.1.1 Lumped element model

Time-dependent heat transfer phenomena can be modelled with lumped element model that is drawn as an equivalent electrical circuit.[33] In this model, the heat source is analogous to the power source, the temperature is analogous to voltage, the heat flux is analogous to electric current, the thermal resistance is analogous to electric resistors, and heat capacity is shown as an electric capacitor. These lumped element models have been used to describe dynamic heat transfer in complex assemblies such as electric motors [34] and microelectronics packages.[35]. The model is well-suited to our calorimeter data analysis since we can use the heater input power and the parameters obtained from a calibration experiment to estimate the heat flux from the sample.[36] This chapter elaborates a lumped element model that illustrates the heat transfer phenomena of the calorimeter highlighted in Chapter 2.

3.1.2 Non-linear regression and Levenberg-Marquardt method

A non-linear regression algorithm was used to estimate the parameters such as heat capacitance and thermal conductance in the lumped-element model using the temperature profiles and input power data obtained from the experiments. The data analysis calculation

was carried out in MATLAB. I provide here a brief introduction of this non-linear regression algorithm.

For any function y that has x as input and a_i as parameters:

$$y = y(x; a_1, a_2, \dots a_M) \tag{1}$$

For a given data set y_i as a function of input x_i with N elements, we can construct a merit function χ^2 to represent the total squared error between the fitted function and the data set:

$$\chi^2 = \sum_{i=1}^{N} \left(\frac{y_i - y(x_i; \boldsymbol{a})}{\sigma_i^2} \right)^2 \tag{2}$$

where $\boldsymbol{a}$ is the vector of the parameter a_i and σ_i is the standard deviation of the data set. In order to minimize χ^2, the critical point of the function must be determined according to the first-order derivative:

$$\frac{\partial \chi^2}{\partial a_k} = 0 \tag{3}$$

Therefore, a vector of first-order derivative functions can be created:

$$\beta_k = \frac{\partial \chi^2}{\partial a_k} = \sum_{i=1}^{N} \frac{y_i - y}{\sigma_i^2} \left(\frac{\partial y}{\partial a_k} \right) \tag{4}$$

We apply Newton's method for solving linear systems of equations to solve for this vector of derivatives. We start by selecting an initial vector value for the parameter $\boldsymbol{a}$. The difference between the next guess and the initial guess can be calculated by solving the following matrix:

$$\sum_{l=1}^{M} \alpha_{kl} \delta a_l = \beta_k \tag{5}$$

Where α_{kl} is an M by M matrix of second-order derivatives of χ^2:

$$\alpha_{kl} = \frac{\partial^2 \chi^2}{\partial a_k \partial a_l} = \sum_{i=1}^{N} \frac{1}{\sigma_i^2} \left(\frac{\partial y}{\partial a_l}\right) \left(\frac{\partial y}{\partial a_k}\right) - \sum_{i=1}^{N} \frac{y_i - y}{\sigma_i^2} \left(\frac{\partial^2 y}{\partial a_k \partial a_l}\right) \quad (6)$$

After solving for δ***a***, we iterate this step with the next ***a*** value as follows:

$$\boldsymbol{a}^{(n+1)} = \boldsymbol{a}^{(n)} + \delta \boldsymbol{a}^{(n)} \quad (7)$$

until the value of ***a*** does not change. A complication is that the required computational power is huge because the size of the matrix is the square of the number of parameters ***a*** and there are hundreds of thousands of data points. The Levenberg-Marquardt algorithm is therefore applied to cut down the steps necessary to converge to the solution. While solving the differential equation system, a 'fudge factor' λ has been used here. Instead of calculating

$$\sum_{l=1}^{M} \alpha_{kl} \delta a_l = \beta_k \quad (5)$$

an alternative system is solved:

$$\sum_{l=1}^{M} \alpha_{kl}' \delta a_l = \beta_k \quad (8)$$

where ***α'*** is the matrix that λ is added to the diagonal values of matrix ***α***:

$$\boldsymbol{\alpha}' = \boldsymbol{\alpha} + \lambda \boldsymbol{I} \quad (9)$$

When λ is large, the diagonal values in the matrix ***α*** dominants the magnitude of the matrix so that the solving procedure is close to the steepest descent algorithm; when λ is close to 0, it is equivalent to solve a typical system of differential equations with Newton's method.

In summary, the parameter estimation protocol by the Levenberg-Marquardt method is:

a) Guess a fitting parameter ***a*** and pick a small value of λ. e.g. $\lambda = 10^{-3}$

b) Solve the system:

$$\sum_{l=1}^{M} \alpha_{kl}{}'\delta a_l = \beta_k$$

for $\delta\boldsymbol{a}$.

c) Compare the merit function of the square error: $\chi^2(\boldsymbol{a} + \delta\boldsymbol{a})$ and $\chi^2(\boldsymbol{a})$.

   i) If $\chi^2(\boldsymbol{a} + \delta\boldsymbol{a}) > \chi^2(\boldsymbol{a})$, we increase λ by a factor of 10 and redo step c) because $\delta\boldsymbol{a}$ is too large a step.

   ii) If $\chi^2(\boldsymbol{a} + \delta\boldsymbol{a}) < \chi^2(\boldsymbol{a})$, we accept the guessed value (a), reduce λ by a factor of 10, and move on to the next modified vactor: $\boldsymbol{a^{n+1}} = \boldsymbol{a^n} + \delta\boldsymbol{a^n}$.

d) Stop the calculation when the χ^2 hardly changes and the difference between two χ^2 smaller than an arbitrary error ε.

3.2 Nonlinear lumped element thermal model of the calorimeter

A two-state nonlinear model has been built to model the heat transfer from the heating coil and the sample to the outer surface of our calorimeter. An equivalent circuit depiction of the model is shown in Fig. 3.1. In this circuit, T_a, T_b and T_s are the measured average temperature of the heating zone (TC1-TC2), firebricks (TC3-TC8) and the outer surface of the isothermal cooling jacket (TC9-TC15), respectively. P_{stored} is the power that is being stored by the calorimeter body and C_i is the total thermal capacitance at a specific position where $i \in \{a, b\}$. The power storage of the calorimeter can be represented using the equation:

$$P_{stored} = C_i\left(\frac{dT}{dt}\right) \tag{10}$$

P_{cond} is the power that is conducted through the fire bricks into the cooling jacket and the environment, where k_{ij} is the thermal conductivity and $i \in \{a, b\}, j \in \{b, s\}$. The power conduction can be modelled using the equation:

$$P_{cond} = k_{ij}\Delta T \tag{11}$$

P_{heater} is the controlled input power from the heater coil. A coefficient $\alpha$is used for the correction because not all of the coil length is located in the heating zone. The power generated or absorbed from the sample P_{sample} does not require a scale factor since the sample is located in the center of the calorimeter. Therefore, for a calibration experiment without a sample, the total overall heat transfer is represented as:

$$\alpha P_{heater} = P_{stored} + P_{cond} \tag{12}$$

By rearranging the equations, the equation above can be written in a differential form:

$$\frac{dT_a}{dt} = \frac{\alpha P_{heater} - k_{ab}(T_a - T_b) - k_{as}(T_a - T_s)}{C_a} \tag{13}$$

$$\frac{dT_b}{dt} = \frac{k_{ab}(T_a - T_b) - k_{bs}(T_b - T_s)}{C_b} \tag{14}$$

Here, the three unknown elements, α, k_{ij} and C_i, are the second-order functions of temperature T_i:

$$\alpha = \alpha_0 + \alpha_1 T_a + \alpha_2 {T_a}^2 \tag{15a}$$

$$k_{ij} = k_{0,i} + k_{1,i} T_i + k_{2,i} {T_i}^2 \tag{15b}$$

$$C_i = C_{0,i} + C_{1,i} T_i + C_{2,i} {T_i}^2 \tag{15c}$$

The unknown elements in each differential equation are estimated utilizing the Leverberg-Marquardt method to fit $\frac{dT}{dt}$ versus *t*. For example, for the second-order parameters α, k_{ij} and C_i, there are 12 unknowns in equation (13) and a 12 by 12 matrix of differential

equations needs to be solved. Typically, for a 12-hour experiment with 15 thermocouples as well as the pressure sensor and power measurements, with one data point per second, the computational power required is not trivial. Therefore, a downsample factor of 60 is used to cut down the data size to one data point per minute. Once the model parameters have been estimated, the thermal power absorbed or generated by the sample can be inferred from temperature data according to the equation:

$$P_{sample} = C_a \frac{\partial T_a}{\partial t} + k_{as}(T_a - T_s) + k_{ab}(T_a - T_b) - \alpha P_{heater} \tag{16}$$

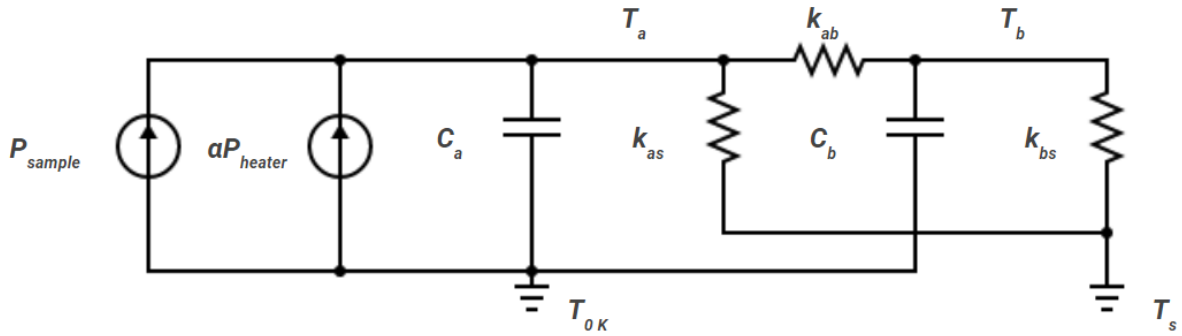

Fig. 3.1 The two-source, two-state, lumped element heat transfer model of the instrument used to infer the sample power from temperature data. The power from heater, P_{heater}, is modelled as the current source with temperature-dependent scale factor, which accounts for the temperature dependence of the radiative and conductive coupling of the heat sources to the sensors. Heat capacitors at the nodes *i* are modelled as capacitors C_i and conductance between nodes *i* and *j* are modelled as conductances k_{ij}.

A typical calorimetric measurement and thermal analysis protocol involves two steps. First, an empty-loaded calibration experiment is carried out with a programmed heating profile. The parameters in the "grey box" are estimated based on the input power and output temperature data using the lumped element heat transfer model and Levenberg-Marquardt method. After the calorimeter cools down to room temperature, a sample experiment is carried out with the same power profile. The time-dependent power P_{sample} is calculated from

equation (16) using the parameters obtained from the calibration experiment. The enthalpy change of the sample is the integration of the power over a certain period of time:

$$\Delta H = \int P_{sample} dt \tag{17}$$

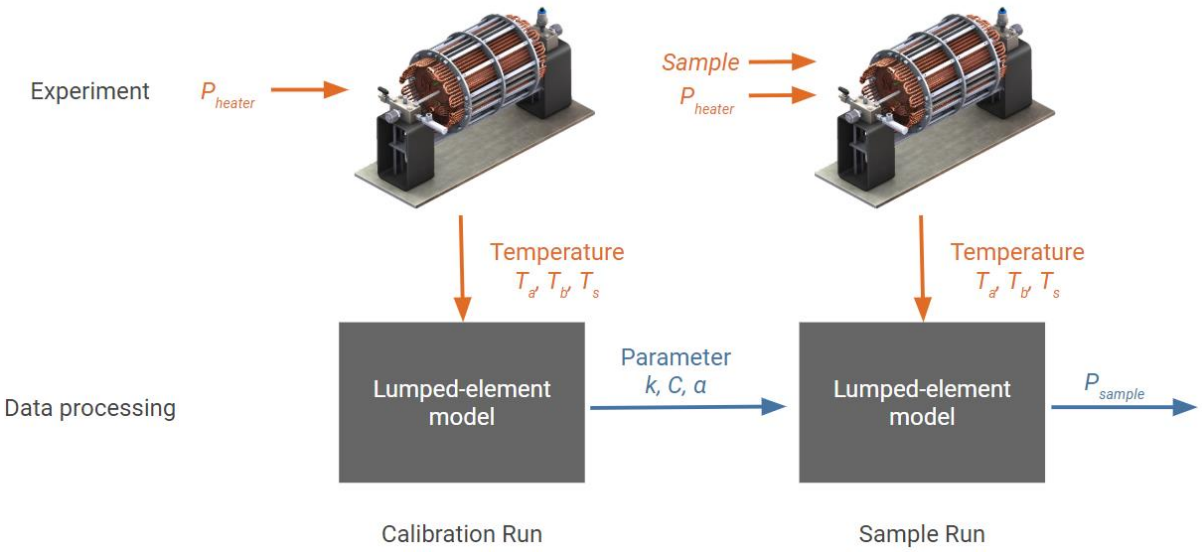

Fig. 3.2 Experiment and thermal analysis protocol. The parameters in the lumped-element model are estimated based on the result from an empty calibration run. The power of the sample generated or absorbed is inferred using the parameters from the calibration run together with the data from the sample run.

In the calibration run, the R^2 goodness-of-fit of experimental temperature profile and the simulated temperature was used to estimate the fitting accuracy. The R^2 is defined in the following equation:

$$R^2 = 1 - \frac{\sum_{t=1}^{N}(T_{i,measured}(t) - T_{i,simulated}(t))^2}{\sum_{t=1}^{N}(T_{i,measured}(t) - \overline{T}_i)^2} \tag{18}$$

3.3 Model validation

3.3.1 Aluminum melting experiment

I conducted an experiment to validate the capability of the instrument to measure the latent heat of fusion of aluminum which is already known. A calibration run that linearly ramped the power from 0 W to 300 W in a period of 12 hours with 1 bar of argon gas in the reaction tube was carried out before the sample run. This input power ramp caused T_a to undergo approximately linear temperature ramps between room temperature and over 1100 °C. The calibration data $\frac{dT}{dt}$was fitted with the Levenberg-Marquardt method and is shown in Fig.3.3 (a). The accuracy of the fit is 99.99% and 99.96% for T_a (TC1-TC2) and T_b (TC5-TC8) based on the R^2 calculation. The parameters were estimated and are listed in Table S2. Fig. 3.3b shows the temperature profile of T_a and T_b and the simulated temperature profile obtained by using the parameters estimated from the lumped element model.

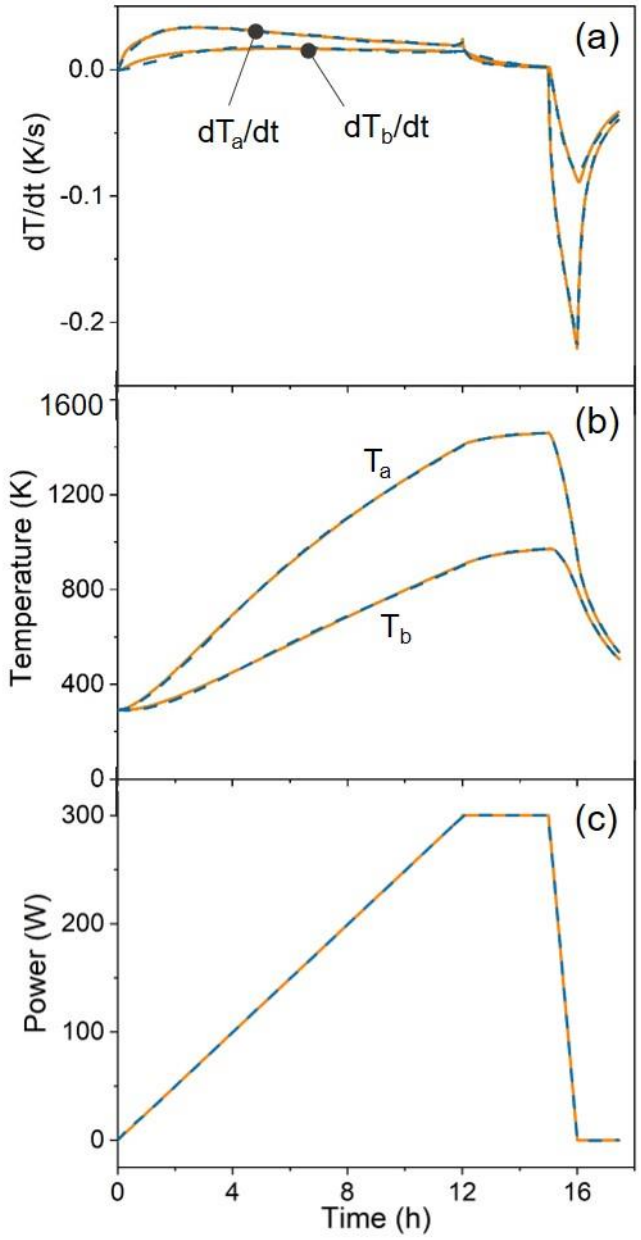

Fig. 3.3 (a) The temperature change rate ($\frac{dT}{dt}$) data (solid orange line) and simulated results (blue dashed line) from the model at different thermocouple positions a (TC1,TC2) and b (TC5-TC8). (b) The temperature profile data (solid orange line) and simulated results (blue dashed line) from the model at different thermocouple positions T_a (solid lines)and T_b (dashed lines). The accuracies (R^2) of the fitting are 99.99% and 99.96% for T_a and T_b, respectively. The heater input power profile data (orange solid line) and simulated results (blue dashed line).

After estimating the model parameters from the calibration experiment, 2.5 g of aluminum powder was added to the alumina crucible that was loaded in the center of the calorimeter. The same power profile was used to heat the calorimeter. The time-dependent sample power is inferred from equation (16). Fig. 3.4 shows an overall negative power profile from the sample and the crucible and also shows a clear peak at around 5 - 6 hours. This was because the crucible and the sample were constantly absorbing heat during the experiment, and the sample absorbed significantly more energy during the melting process. The baseline subtraction can enable the integration of a calorimetric peak on top of a large instrumental baseline with some degree of accuracy if the peak is sufficiently distinct from the baseline. To calculate the heat required to melt the aluminum in this present case, a baseline power profile was first linearly interpolated based on the beginning and endpoints of the melting peak. (Fig. 3.4) The area between the baseline and the peak was then numerically integrated and the result was 992.2 J, which is very close to the theoretical heat required to melt 2.5g of aluminum, 987.04 J.

Although the result from the peak area integration seems extremely accurate, it still might be a coincidence. The evidence is that the beginning and end temperatures of this melting peak, recorded by the thermocouples in the heating zone (TC1, TC2), are 828.5 K and 918.7 K. Based on the COMSOL model, the center of the reaction tube was only ~10 K hotter than the heating zone. Aluminum, however, melts at 933 K and no peak was shown around that temperature. One possible explanation is that the center of the calorimeter is significantly hotter with the presence of the sample than an empty loaded calibration run because solid-solid heat conduction transfers heat faster than the argon gas in the tube being heated by radiation and convection. One possible improvement of the calorimeter is to

anchor a thermocouple right next to the sample in the reaction tube so that the real melting temperature can be captured. This improvement, however, can only be used in a non-oxidative and non-corrosive environment.

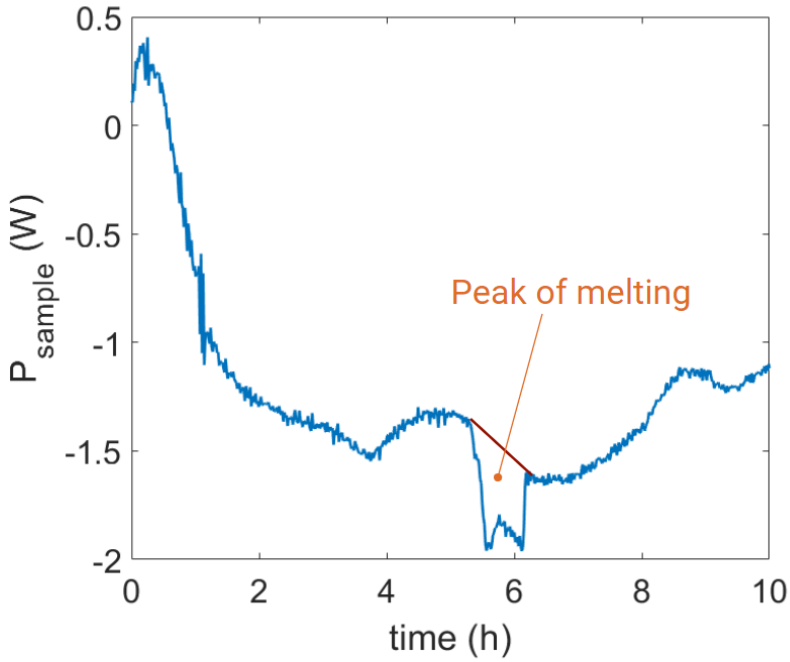

Fig. 3.4 The inferred power of sample from the 2.5 g aluminum heat of fusion measurement. A quite clear peak is shown and implies the melting process. A baseline is interpolated and subtracted from the peak so that the area between the peak and the baseline can be integrated. The calculated melting enthalpy change is 992.2 J, compared with a theoretical value of 987.04 J.

3.3.2 Calorimetry of a simulated exothermic process

We conducted an experiment simulating exothermic processes at the sample location at several different temperatures using the calibration heater. The calibration heater is a Kanthal A1 resistance wire that is tightly wound on an alumina crucible which is anchored in the middle of the reaction tube. (Fig. S1) The calibration heater is controlled by a separate

power source to simulate exothermic power pulses. In this experiment, the main heater input power was ramped linearly from 0 W to 350 W and back to 0 W symmetrically over the course of 10 hours. This input power ramp caused T_a to undergo approximately linear temperature ramps between room temperature and 1114 °C. During this time, an exothermic process at the sample location was simulated by switching the input power to the calibration heater between 0 W and 1 W for 15-minute periods (corresponding to 900 J exotherms).

The power inputs are plotted in Fig. 3.3 (a). The inferred calibration heater power during the experiment is plotted in Fig. 3.3 (b). Fig. 3.3 (b) shows that the 900 J / 1 W heater pulses can be recovered but with only approximately 50% of the amplitude. I attributed this mismatch to the limitations associated with the lumped element model. In my two-source and two-state model, the sample power is assumed to be 100% transferred out of or be stored by the instrument but is not considered to heat the sample itself. In this sense, the calibration heater with non-negligible thermal mass should be considered as a thermal capacitance as well. The alumina parts in the calibration heater absorbed heat from the heater wire itself so that the power pulses were not fully captured by the thermocouples that were mounted outside of the reaction tube. Therefore, other than improving the physical configuration of the calorimeter by anchoring an additional thermocouple in the reaction tube right next to the sample, I can also improve the lumped heat model by employing a scale factor β ($0 < \beta < 1$) for the sample power. The value of β represents the percentage of the power that transferred out of the sample to the calorimeter body. The sample power can then be calculated using the equation:

$$P_{sample} = \frac{1}{\beta}\left[C_a \frac{d}{dt}T_a + k_{as}(T_a - T_s) + k_{ab}\,(T_a - T_b) - \alpha P_{heater}\right] \quad (18)$$

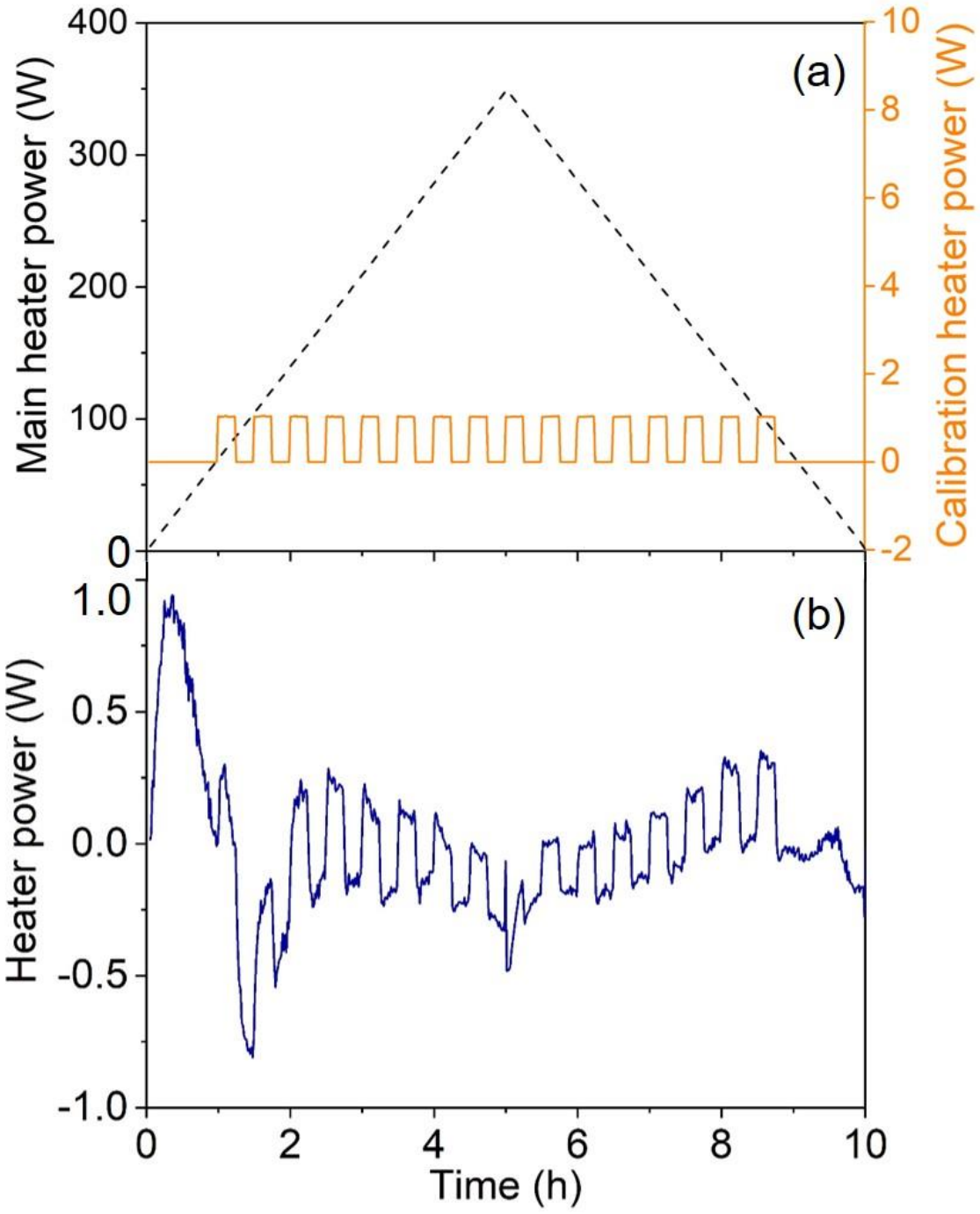

Fig. 3.5 Summary of calorimetric data from the exothermal simulation experiment. (a) The input powers to the main and calibration heaters. (b) The calibration heater power as inferred using the calibration run. The input power pulses are clearly recovered but with much lower amplitude. One

possible reason is the since the calibration heater has a relatively large mass, it acts as a heat sink that can absorb part of the power from the calibration heater.

3.4 Conclusion

A nonlinear, lumped-parameter heat transfer model of the instrument, with parameter values estimated using grey-box system identification techniques and calibration data, was used to infer heat flux at the sample position from experimental temperature data. This technique grants much more freedom in the geometric configuration of the sample, heater, and sensors than calorimetry schemes that employ a single calibration factor. While the instrument geometry and model must both be clearly optimized to achieve high accuracy, this concept of model-based calorimetry can enable calorimetric measurements to be performed when practical constraints preclude the application of more conventional calorimetric techniques. Two validation experiments were carried out and they demonstrated that this model was able to capture the enthalpy change signals of the fusion of 2.5 g aluminum powder as well as the exothermic simulation from a calibration heater. Possible improvements, such as employing another scale factor for the sample power sources, can be made for this model to obtain better results.

Chapter 4: Conclusion and future direction

Part of the content under “future directions” is published in the paper MacLeod *et al.*, *Review of Scientific Instruments*, **88**, 084101 (2017).

4.1 Conclusion

In order to study metal hydride thermodynamics and kinetics at high-temperatures and high-pressures for thermochemical energy storage applications, I have contributed to the design and fabrication of a novel calorimeter that is capable of operating up to at least 1232 °C while under pure hydrogen pressures up to 33 bar. This thesis highlights the physical design of the calorimeter, a finite element analysis model of the heat transfer phenomena in Chapter 2. Chapter 3 elaborates a two-source, two-state lumped element model that was constructed to calculate the heat generation or absorption by the chemical in the calorimeter from the data of input power and output temperatures.

The key design concept of this calorimeter is to keep the sample in a well-insulated environment with a well-controlled surface temperature so that the power generated or absorbed by the sample can be sensitively detected. In our design, the fire bricks provide heat insulation and a copper isothermal cooling jacket cooled by a chiller is used to control the surface temperature. The temperature profile can be predicted by the model before carrying out any experiment using the finite element analysis (FEA) model constructed with COMSOL. Both the model and the calibration experiment suggested that with 350 W input power, the temperature of the heating zone is able to reach 1281.8 °C. Furthermore, the lumped-element model provides a useful tool to infer the power and enthalpy of the

chemicals. This methodology grants more freedom to the geometric configuration of the calorimeter, sample and the sensors by estimating heat transfer parameters from a single calibration experiment.

4.2 Future direction

Here we identify possible future improvements to our apparatus and refinements to the data analysis procedures that may be of utility to interested workers. In particular, the calorimetric accuracy can be improved and increased operating pressures and temperatures should be possible.

1. Improving the mechanical stability of the instrument, especially the poorly constrained tip positions of the most important thermocouples, TC1 and TC2, to minimize run-to-run physical variations should improve the reproducibility of the calibration and therefore the accuracy of the measurement.
2. The calorimetric accuracy could be improved by a modified furnace configuration wherein the heater power is used to heat an isothermal boundary which surrounds the sample and temperature sensors. This proposed approach is similar to contemporary differential scanning calorimeters except that the differential measurement is taken through subsequent apparatus runs. In such a configuration, the furnace wall between the heater and the sample tube becomes the thermal ground in the lumped element model, and fewer model parameters would be required because the heater power input and the model elements associated with the thermal mass and thermal conductances of the furnace vanish from the model. The simpler resulting model would deal only with

the dynamics of the heat fluxes from the sample through the sensor(s) to the furnace wall and the slow heat fluxes through the furnace insulation need not be modelled at all.

3. Improved estimates of the model parameters might also be obtained by using optimized calibration routines rather than heuristically chosen ones.[37]
4. High-temperature operation at pressures well beyond 33 bars should be possible with a reaction tube of low-porosity alumina or another suitable material. Our simple pressure vessel calculations predict a rupture pressure of 221 bars for the alumina reaction tube employed, although a more accurate prediction of rupture pressure would consider stresses induced by temperature gradients and defects in the alumina.[38]
5. The maximum operating temperature of the presented design is limited by the melting point of the resistive heater, which can be readily replaced with a silicon carbide heater suitable for operation up to 1650 °C.
6. At lower operating pressures, we have had preliminary success using a quartz reaction tube that provides optical access to the sample under investigation.
7. Higher-pressure and lower-temperature operation should also be feasible with metal reaction tubes (e.g., steel and Hastelloy) as demonstrated by Zuttel and coworkers.[30]

The instrument presented here will provide information on the thermodynamics and kinetics on a range of candidate heterogeneous chemical reactions for emerging applications. This instrument will be useful in characterizing thermochemical energy storage systems utilizing metal hydrides that a large number of those systems operate between 300 °C and 1150 °C (e.g. MgH_2, Mg_2FeH_6, NaH, $NaBH_4$, LiH, CaH_2, ScH_x, $NaMgH_3$, $Ca_4Mg_4Fe_3H_{22}$, $CaMgNiH_4$).[14]

The calorimeter presented in this work may also find use in other fields that utilize heterogeneous chemical reactions at elevated temperature and pressure. For example, chemical looping combustion (CLC) is a technique that utilizes metal oxide dissociation at high temperatures (860 - 1200 °C) to produce oxygen gas that can subsequently react with fossil fuels in a "fuel reactor" producing pure carbon dioxide.[39] The reduced metal oxides or pure metal can be then cycled back in an "air reactor" to be re-oxidized to form metal oxides. In a CLC process, the metal oxides, also known as "oxygen carrier" in this technique, undergo cycles of decomposition and re-oxidation in air or with the fuel. The CLC process gives a solution to capture pure carbon dioxide from its source and can be adapted by conventional fossil fuel power plants. (Fig. 4.1) Knowing the reaction kinetics, thermodynamics, material cyclability, effect of attrition and agglomeration is crucial for the design of a CLC system.

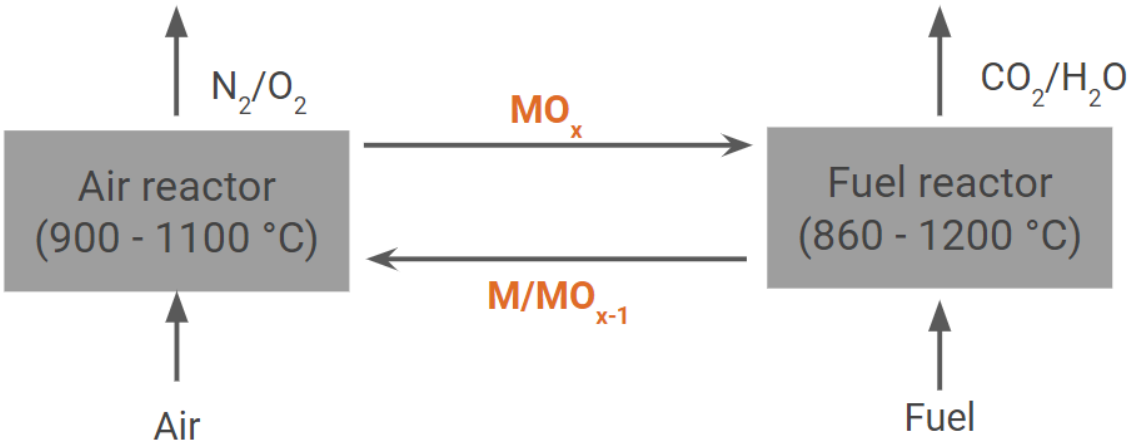

Fig. 4.1 Schematic of the chemical looping combustion process. Metals or metal oxides (M/MO_{x-1} in the figure) with lower oxidation number react with air to form metal oxides (MO_x) in the air reactor. The resultant metal oxides are then sent to the fuel reactor to react with fuel and produce carbon dioxide and water. The reduced metal oxides are cycled back to the air reactor to be re-oxidized. The

CLC process gives a solution to capture pure carbon dioxide from its source and can be adapted by conventional fossil fuel power plants.

The calorimeter presented in this thesis can be used in two ways to study metal oxides, such as CuO, Mn_3O_4, Co_3O_4 and their alloys, for CLC systems. First, the instrument is capable of obtaining information of metal oxide reactions at high-temperature and high-pressure. The high-pressure condition can increase the gas conversion efficiency for some metal ores that used as "oxygen carriers". [40] For example, in an experiment that reacting an iron ore as the oxygen carrier with bituminous coal at 6 bar and 970 ^oC, higher CO_2 concentration and lower CH_4, H_2 and CO concentration was observed.[41] Second, with modifications on the instrument, which involves two mass flow controllers and an outlet to gas chromatography (GC), our calorimeter will be capable of studying the decomposition reactions of metal oxides at a constant pressure. (Fig. 4.2)

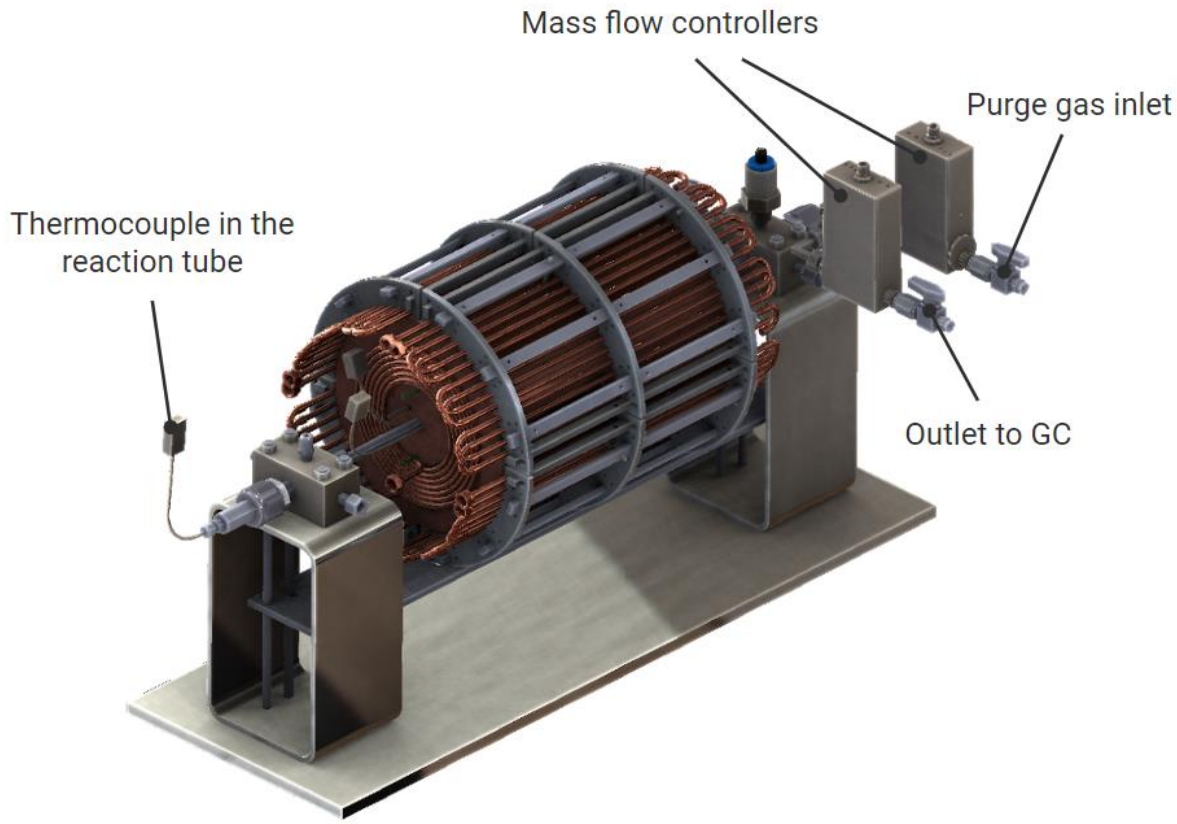

Fig. 4.2 A modification of the calorimeter. Two mass flow controllers are added to one of the gas sealing manifolds. The inner gas can be purged in through one mass flow controller and the other one can lead the outlet gas to GC for gas composition analysis. This modification enables the study of the reactions at a controlled pressure.

The calorimeter presented in this thesis can also be utilized to investigate the claims in low-energy nuclear reaction (LENR), also known as 'cold fusion'.[42] One prominent claim in LENR states that certain metallic powder produced excess heat when heated in the hydrogen environment, which is attributed to the nuclear reaction by the researchers in this field.[43] These experiments, which were carried out at extreme conditions (<1400 ^{o}C), apparently would require careful measurements with suitably designed, fabricated and calibrated instrumentation. We tested 420 samples to evaluate claims of excess heat produced by Ni-H material systems in our calorimeter using the heat transfer model. The independent

variables we tested included temperature, pressure, sample composition, particle sizes, surface treatment, and others.[42] We did not observe any evidence of excess heat from the 420 samples we evaluated. While we might not recreated the experimental conditions claimed to generate excess heat, this thesis presents a calorimeter and analytical tool that may provide value to those who are interested in evaluating this parameter space.

References

(1) MacLeod, B. P.; Schauer, P. A.; Hu, K.; Lam, B.; Fork, D. K.; Berlinguette, C. P. High-Temperature High-Pressure Calorimeter for Studying Gram-Scale Heterogeneous Chemical Reactions. *Rev. Sci. Instrum.* **2017**, *88* (8), 084101.

(2) Pardo, P.; Deydier, A.; Anxionnaz-Minvielle, Z.; Rougé, S.; Cabassud, M.; Cognet, P. A Review on High Temperature Thermochemical Heat Energy Storage. *Renewable Sustainable Energy Rev.* **2014**, *32*, 591–610.

(3) Denholm, P.; King, J. C.; Kutcher, C. F.; Wilson, P. P. H. Decarbonizing the Electric Sector: Combining Renewable and Nuclear Energy Using Thermal Storage. *Energy Policy* **2012**, *44*, 301–311.

(4) Citation, S. 2018 U.S. Utility-Scale Photovoltaics- Plus-Energy Storage System Costs Benchmark Ran Fu, Timothy Remo, and Robert Margolis.

(5) Alva, G.; Lin, Y.; Fang, G. An Overview of Thermal Energy Storage Systems. *Energy* **2018**, *144*, 341–378.

(6) Richard. Round Trip Efficiency in Batteries: A Critical Matter - News about Energy Storage, Batteries, Climate Change and the Environment https://www.upsbatterycenter.com/blog/round-trip-efficiency-batteries/ (accessed Jul 30, 2019).

(7) Sioshansi, R.; Denholm, P. The Value of Concentrating Solar Power and Thermal Energy Storage. *IEEE Transactions on Sustainable Energy* **2010**, *1* (3), 173–183.

(8) Mileva, A.; Nelson, J. H.; Johnston, J.; Kammen, D. M. SunShot Solar Power Reduces Costs and Uncertainty in Future Low-Carbon Electricity Systems. *Environ. Sci. Technol.* **2013**, *47* (16), 9053–9060.

(9) Chen, H.; Cong, T. N.; Yang, W.; Tan, C.; Li, Y.; Ding, Y. Progress in Electrical Energy Storage System: A Critical Review. *Prog. Nat. Sci.* **2009**, *19* (3), 291–312.

(10) van der Linden, S. Bulk Energy Storage Potential in the USA, Current Developments and Future Prospects. *Energy* **2006**, *31* (15), 3446–3457.

(11) Kuravi, S.; Trahan, J.; Goswami, D. Y.; Rahman, M. M.; Stefanakos, E. K. Thermal Energy Storage Technologies and Systems for Concentrating Solar Power Plants. *Prog. Energy Combust. Sci.* **2013**, *39* (4), 285–319.

(12) Harries, D. N.; Paskevicius, M.; Sheppard, D. A.; Price, T. E. C.; Buckley, C. E. Concentrating Solar Thermal Heat Storage Using Metal Hydrides. *Proc. IEEE* **2012**, *100* (2), 539–549.

(13) Ulvestad, A. A Brief Review of Current Lithium Ion Battery Technology and Potential Solid State Battery Technologies. *arXiv [physics.app-ph]*, 2018.

(14) Sheppard, D. A.; Paskevicius, M.; Humphries, T. D.; Felderhoff, M.; Capurso, G.; Bellosta von Colbe, J.; Dornheim, M.; Klassen, T.; Ward, P. A.; Teprovich, J. A.; et al. Metal Hydrides for Concentrating Solar Thermal Power Energy Storage. *Appl. Phys. A: Mater. Sci. Process.* **2016**, *122* (4), 395.

(15) Wentworth, W. E.; Chen, E. Simple Thermal Decomposition Reactions for Storage of Solar Thermal Energy. *Solar Energy* **1976**, *18* (3), 205–214.

(16) Felderhoff, M.; Bogdanović, B. High Temperature Metal Hydrides as Heat Storage Materials for Solar and Related Applications. *Int. J. Mol. Sci.* **2009**, *10* (1), 325–344.

(17) Paskevicius, M.; Sheppard, D. A.; Buckley, C. E. Thermodynamic Changes in Mechanochemically Synthesized Magnesium Hydride Nanoparticles. *J. Am. Chem. Soc.* **2010**, *132* (14), 5077–5083.

(18) Zaluska, A.; Zaluski, L.; Ström–Olsen, J. O. Nanocrystalline Magnesium for Hydrogen Storage. *J. Alloys Compd.* **1999**, *288* (1), 217–225.

(19) Bogdanović, B.; Hartwig, T. H.; Spliethoff, B. The Development, Testing and Optimization of Energy Storage Materials Based on the MgH2 Mg System. *Int. J. Hydrogen Energy* **1993**, *18*

(7), 575–589.
(20) Reiser, A.; Bogdanović, B.; Schlichte, K. The Application of Mg-Based Metal-Hydrides as Heat Energy Storage Systems. *Int. J. Hydrogen Energy* **2000**, *25* (5), 425–430.
(21) Zhang, X.; Tian, W.; Yang, J.; Yang, R.; Zheng, J.; Li, X. Synthesis and Hydrogen Storage Behaviour of Pure Mg2FeH6 at Nanoscale. *Mater. Trans.* **2011**, *52* (4), 618–622.
(22) Aronson, S.; Salzano, F. J. Solid-State Reaction of Lithium Hydride and Aluminum. *Inorg. Chem.* **1969**, *8* (7), 1541–1542.
(23) Vajo, J. J.; Mertens, F.; Ahn, C. C.; Bowman, R. C.; Fultz, B. Altering Hydrogen Storage Properties by Hydride Destabilization through Alloy Formation: LiH and MgH2 Destabilized with Si. *J. Phys. Chem. B* **2004**, *108* (37), 13977–13983.
(24) Abbas, M. A.; Grant, D. M.; Brunelli, M.; Hansen, T. C.; Walker, G. S. Reducing the Dehydrogenation Temperature of Lithium Hydride through Alloying with Germanium. *Phys. Chem. Chem. Phys.* **2013**, *15* (29), 12139–12146.
(25) Jain, A.; Miyaoka, H.; Ichikawa, T.; Kojima, Y. Correlation between Electrochemical Behavior and Hydrogen Storage Properties of Li–Sn System. *J. Alloys Compd.* **2013**, *580*, S211–S215.
(26) Javadian, P.; Sheppard, D. A.; Jensen, T. R.; Buckley, C. E. Destabilization of Lithium Hydride and the Thermodynamic Assessment of the Li–Al–H System for Solar Thermal Energy Storage. *RSC Adv.* **2016**, *6* (97), 94927–94933.
(27) Bogdanović, B.; Reiser, A.; Schlichte, K.; Spliethoff, B.; Tesche, B. Thermodynamics and Dynamics of the Mg–Fe–H System and Its Potential for Thermochemical Thermal Energy Storage. *J. Alloys Compd.* **2002**, *345* (1), 77–89.
(28) 96 Line TGA, large volume & high temperature thermogravimetry - Setaram https://www.setaram.com/setaram-products/thermal-analysis/thermogravimetry-tga/96-line-tga/ (accessed Aug 13, 2019).
(29) Long, X. F.; Dai, L.; Lou, B.; Wu, J. The Kinetics Research of Thermochemical Energy Storage System Ca(OH) 2 /CaO : Kinetics Research Thermochemical Energy Storage. *Int. J. Energy Res.* **2017**, *41* (7), 1004–1013.
(30) Mauron, P.; Bielmann, M.; Bissig, V.; Remhof, A.; Züttel, A. High-Pressure and High-Temperature Differential Scanning Calorimeter for Combined Pressure-Concentration-Temperature Measurements of Hydrides. *Rev. Sci. Instrum.* **2009**, *80* (9), 095113.
(31) André, L.; Abanades, S.; Flamant, G. Screening of Thermochemical Systems Based on Solid-Gas Reversible Reactions for High Temperature Solar Thermal Energy Storage. *Renewable Sustainable Energy Rev.* **2016**, *64*, 703–715.
(32) Chłopek, K.; Frommen, C.; Léon, A.; Zabara, O.; Fichtner, M. Synthesis and Properties of Magnesium Tetrahydroborate, Mg(BH4)2. *J. Mater. Chem.* **2007**, *17* (33), 3496–3503.
(33) Sidebotham, G. *Heat Transfer Modeling: An Inductive Approach*; Springer, Cham, 2015.
(34) Okoro, O. I. Steady and Transient States Thermal Analysis of a 7.5-kW Squirrel-Cage Induction Machine at Rated-Load Operation. *IEEE Trans. Energy Convers.* **2005**, *20* (4), 730–736.
(35) Christiaens, F.; Vandevelde, B.; Beyne, E.; Mertens, R.; Berghmans, J. A Generic Methodology for Deriving Compact Dynamic Thermal Models, Applied to the PSGA Package. *IEEE Trans. Compon. Packag. Manuf. Technol. Part A:* **1998**, *21* (4), 565–576.
(36) Ljung, L. System Identification, Theory for the User, Information and System Science Series. *Englewood Cliffs* **1987**.
(37) Goodwin, G. C. Optimal Input Signals for Nonlinear-System Identification. *Proceedings of the Institution of Electrical Engineers* **1971**, *118* (7), 922–926.
(38) Abe, H.; Naito, M.; Hotta, T.; Shinohara, N.; Uematsu, K. Flaw Size Distribution in High-Quality Alumina. *J. Am. Ceram. Soc.* **2003**, *86* (6), 1019–1021.
(39) Li, J.; Zhang, H.; Gao, Z.; Fu, J.; Ao, W.; Dai, J. CO2 Capture with Chemical Looping Combustion of Gaseous Fuels: An Overview. *Energy Fuels* **2017**, *31* (4), 3475–3524.
(40) Wang, P.; Means, N.; Shekhawat, D.; Berry, D.; Massoudi, M. Chemical-Looping Combustion and Gasification of Coals and Oxygen Carrier Development: A Brief Review. *Energies* **2015**, *8*

(10), 10605–10635.
(41) Xiao, R.; Song, Q.; Zhang, S.; Zheng, W.; Yang, Y. Pressurized Chemical-Looping Combustion of Chinese Bituminous Coal: Cyclic Performance and Characterization of Iron Ore-Based Oxygen Carrier. *Energy Fuels* **2010**, *24* (2), 1449–1463.
(42) Berlinguette, C. P.; Chiang, Y.-M.; Munday, J. N.; Schenkel, T.; Fork, D. K.; Koningstein, R.; Trevithick, M. D. Revisiting the Cold Case of Cold Fusion. *Nature* **2019**, *570* (7759), 45–51.
(43) Focardi, S.; Habel, R.; Piantelli, F. Anomalous Heat Production in Ni-H Systems. *Nuovo Cimento: C: Geophys. Space Phys.* **1994**, *107* (1), 163–167.
(44) Pagkoura, C.; Karagiannakis, G.; Zygogianni, A.; Lorentzou, S.; Kostoglou, M.; Konstandopoulos, A. G.; Rattenburry, M.; Woodhead, J. W. Cobalt Oxide Based Structured Bodies as Redox Thermochemical Heat Storage Medium for Future CSP Plants. *Solar Energy* **2014**, *108*, 146–163.
(45) Gennari, F. C.; Castro, F. J.; Andrade Gamboa, J. J. Synthesis of Mg2FeH6 by Reactive Mechanical Alloying: Formation and Decomposition Properties. *J. Alloys Compd.* **2002**, *339* (1), 261–267.
(46) Spriggs, R. M.; Mitchell, J. B.; Vasilos, T. Mechanical Properties of Pure, Dense Aluminum Oxide as a Function of Temperature and Grain Size. *J. Am. Ceram. Soc.* **1964**, *47* (7), 323–327.
(47) Irfan, M. A.; Chapman, W. Thermal Stresses in Radiant Tubes due to Axial, Circumferential and Radial Temperature Distributions. *Appl. Therm. Eng.* **2009**, *29* (10), 1913–1920.

Appendices

Appendix A. Supplemental information for Chapter 2.

Appendix A is the part of the supplementary material of the paper High-temperature and high-pressure calorimeter for studying gram-scale heterogeneous reactions (MacLeod *et al*., *Review of Scientific Instruments* **88**, 084101 (2017))

Manufacturer	Model	Maximum operating temperature	Maximum operating pressure	Maximum partial pressure of hydrogen
Linseis	STA HP/1	1000 °C	150 bar	7.5 bar
Linseis	STA HP/2	1800 °C	50 bar	2.5 bar
Mettler Toledo	HP DSC 2+	700 °C	100 bar	100 bar
Netzsch	DSC 204 Phoenix	450 °C	150 bar	150 bar
Perkin Elmer	DSC 8000 + pressure cell accessory	750 °C	41 bar	41 bar

Table S1. Summary of specifications of commercially available high temperature/pressure calorimeters (Reproduced from MacLeod *et al*., *Review of Scientific Instruments* **88**, 084101 (2017), with the permission of AIP Publishing)

Design objectives

To enable a wide range study on heterogeneous chemical reactions relevant to thermochemical energy storage (TES) and other applications, we set out to develop an instrument that could perform simultaneous calorimetric and pressure measurements on gram-scale solid samples at elevated temperatures under high pressures of pure hydrogen. This section details our quantitative design objectives and our rationale for their selection.

Operating temperature 1300 °C: A large number of metal hydride systems operate between 300 °C and 1150 °C (e.g. MgH_2, Mg_2FeH_6, NaH, $NaBH_4$, LiH, CaH_2, ScH_x, $NaMgH_3$,

$Ca_4Mg_4Fe_3H_{22}$, $CaMgNiH_4$).[14] We chose to design for a maximum operating temperature of 1300 °C to enable studies on these and other systems and to avoid operating too close to the 1400 °C temperature limit of the highest temperature resistance-heating alloy readily available, Kanthal® A-1

Operating pressure 50 bar: The equilibrium pressures for TES materials over their working temperature ranges approach 100 bar (for MgH_2 at 500 °C) [16]and pilot-scale MgH_2 TES systems operating at hydrogen pressures up to 50 bar have been implemented.[27]

Sample volume 10 mL / >1 gram: In TES pilot plants, kg quantities of reactant solids are employed.[27] With such large volumes of material, special measures must be taken to permit gas phase reactants to quickly and fully react with the solids. One approach that enhances gas-phase access to the solid is to press the powders into perforated, flow-through pellets with dimensions of millimeters and masses of several grams.[40] A large sample volume can accommodate either pellets or powders. Large samples also produce large barometric and calorimetric signals, reducing the difficulty of making measurements with the adequate signal to noise ratios and providing ample material for post-heating analyses.

Calorimetric resolution<100mW: Gennari and coworkers show differential scanning calorimetry data employing typical calorimetric ramp rates for the Mg_2FeH_6 system where the sample power is of order 1 W/g.[41] To clearly resolve such calorimetric events for our intended gram-scale samples, a calorimetric resolution much less than 1 W is therefore required.

Calorimetric accuracy <10%: Due to the large size of the samples to be employed with this instrument, achieving highly accurate measurements of absolute heats of the reaction was anticipated to be difficult due to thermal gradients within the sample. 10% calorimetric

accuracy was deemed to be adequate to verify the nature of reactions taking place by comparison of reaction heats with established thermodynamic data, and also to identify any physical processes (such as melting) which are not coupled to pressure changes.

Pressure measurement resolution 0.02 bar: A 1 g sample of MgH_2 contains 76 mmol of hydrogen gas, the release of which into a 1 L volume at 300 K will cause a pressure change of approximately $\Delta P = \frac{\Delta nRT}{V} = \frac{(0.076)\,(8.314)(300)}{0.001}\ pa \approx 2\ bar$. Because the instrument presented here will operate at elevated temperature and have gas volume <1 L, 2 bar is a conservative underestimate of the magnitude of the expected pressure changes from typical experiments. A pressure measurement which can resolve 1% of this estimated pressure change (i.e. 0.02 bar) should, therefore, be adequate for tracking the formation and decomposition of hydrides.

Notes on pressure vessel design

Simple pressure vessel design calculations we performed, which take into account the decrease in mechanical strength of alumina at elevated temperatures,[42] predict rupture of the alumina reaction tube by tensile failure at 221 bar internal pressure when the tube is at 1300 °C. Although not considered in our calculations, additional stresses can arise due to nonlinear temperature gradients along the reaction tube axis[43] which will act to reduce the rupture pressure. The quality of the alumina is crucial to its strength, as the strength of this material has been found to be controlled by the size of the largest defects in the material.[38]

Appendix B. Supplemental information for Chapter 3.

Part of Appendix B is from the supplementary material of the paper High-temperature and high-pressure calorimeter for studying gram-scale heterogeneous reactions (MacLeod *et al*., *Review of Scientific Instruments* **88**, 084101 (2017))

Fig. S1. Photograph of the calibration heater and a tubular alumina crucible. The calibration heater and its leads are formed from a continuous length of Kanthal A1 resistance wire. Each of the two leads has a resistance of approximately 2.7Ω while the leads and coil combined have a resistance of approximately 33Ω. Thus only 83.6% of the nominal power dissipated in the heater is dissipated in the coil. The measurement of the power dissipated in the calibration heater could be made more accurate through the use of 4-wire power measurement and/or heater current supply leads to having lower resistance. (Reproduced from MacLeod *et al*., *Review of Scientific Instruments* **88**, 084101 (2017), with the permission of AIP Publishing)

Parameter	Constant sub-parameter (α_0, $C_{i,0}$, $k_{ij,0}$)	Linear sub-parameter (α_1, $C_{i,1}$, $k_{ij,1}$)	Parabolic sub-parameter (α_2, $C_{i,2}$, $k_{ij,2}$)
α	0.5728	-1.3360e-04 K^{-1}	1.0316e-07 K^{-2}
C_a	309.0768 JK^{-1}	-0.3468 JK^{-2}	1.6042e-04 JK^{-3}
C_b	-369.7279 JK^{-1}	4.9451 JK^{-2}	-0.0039 JK^{-3}
k_{ab}	0.0777 WK^{-1}	1.9865e-04 WK^{-2}	-2.1917e-08 WK^{-3}
k_{as}	0.0755 WK^{-1}	-1.8349e-04 WK^{-2}	9.9043e-08 WK^{-3}
k_{bs}	-0.0099 WK^{-1}	6.2375e-04 WK^{-2}	-3.8835e-07 WK^{-3}

Table S2. Summary of the model parameters reported by the MATLAB lumped heat model code.

MATLAB code for thermal analysis of the lumped element model

```
clc
clear all

%% calculate coefficient vectors a and b

% read data from the calibration data file
[num,txt,raw] = xlsread('Calibration run');
time = raw(2:end, 2);
Ta_data = raw(2:end,3);
Tb_data = raw(2:end,4);
Ts_data = raw(2:end,5);
Pin_data = raw(2:end,6);
downsize = 60;

t = downsample(cell2mat(time),downsize,1);
Ta_data = downsample(cell2mat(Ta_data),downsize,1) + 273;
Tb_data = downsample(cell2mat(Tb_data),downsize,1) + 273;
Ts_data = downsample(cell2mat(Ts_data),downsize,1) + 273;
Pin_data = downsample(cell2mat(Pin_data),downsize,1);
k = numel(t);

clear num

a = sym ('a', [1, 12]);
b = sym ('b', [1,6]);
Ts = 290;
Rate = 300/12/60/60;

% calculate the derivative of temperature over time
for i = 1:k-2
    dTa_data(i) = (Ta_data(i+1)-Ta_data(i))/(t(i+1)-t(i));
end
dTa_data = dTa_data';

for i = 1:k-2
    dTb_data(i) = (Tb_data(i+1)-Tb_data(i))/(t(i+1)-t(i));
end
dTb_data = dTb_data';

% define differential function of temperature at position 'a' and initial
guess of the coefficients
dTa = ((a(1)+a(2)*Ta_data(1:k-2)+a(3)*Ta_data(1:k-2).^2).*Pin_data(1:k-
2)...
    - (a(4)+a(5)*Ta_data(1:k-2)+a(6)*Ta_data(1:k-2).^2).*(Ta_data(1:k-
2) ...
    - Ts_data(1:k-2))-(a(7)+a(8)*Ta_data(1:k-2)+a(9)*Ta_data(1:k-
2).^2).*...
    (Ta_data(1:k-2)- Tb_data(1:k-2))./(a(10)+a(11)*Ta_data(1:k-
2)+a(12)*...
    Ta_data(1:k-2).^2);
```

```
a_coe = [ 0.5728   -0.0001    0.0000    0.0755   -0.0002    0.0000 ...
    0.0777    0.0002   -0.0000  309.0768   -0.3468    0.0002];

b_coe = [-0.0099    0.0006   -0.0000 -369.7279    4.9451   -0.0039];

% calculate coefficient vector 'a' with LM method
a_coe = LMmethod(t, dTa_data, dTa, a, a_coe)

% define differential funcion of temperature at position 'b'
dTb = ((a_coe(7)+a_coe(8)*Ta_data(1:k-2)+a_coe(9)*Ta_data(1:k-2).^2).*...
    (Ta_data(1:k-2)- Tb_data(1:k-2))-(b(1)+b(2)*Tb_data(1:k-2)+b(3)*...
    Tb_data(1:k-2).^2).*(Tb_data(1:k-2)- Ts_data(1:k-2))./(b(4)+b(5)*...
    Tb_data(1:k-2)+b(6)* Tb_data(1:k-2).^2);

% calculate coefficient vector 'b' with LM method
b_coe = LMmethod(t, dTb_data, dTb, b, b_coe)

% figure of dT/dt data and fitted results
figure(1)
plot(t(1:k-2)/60/60, vpa(subs(dTa, a, a_coe)),'color',
[.27 .45 .64],'LineWidth', 3)
set(gca, 'FontSize', 22);
xlabel('hour (s)')
ylabel('dT/dt (K/s)')
hold on
plot(t(1:k-2)/60/60, dTa_data, 'color',[.88 .42 .15] , 'LineWidth', 3)
plot(t(1:k-2)/60/60, vpa(subs(dTb, b, b_coe)),'-.', 'color',
[.27 .45 .64],'LineWidth', 3)
plot(t(1:k-2)/60/60, dTb_data, '-.', 'color',[.88 .42 .15] , 'LineWidth',
3)
legend('dTa/dt inffered', 'dTa/dt data', 'dTb/dt inffered', 'dTb/dt data')

%% Use numetrical method to determine how well it fits the calibration
% using initial temperature values at position 'a' and 'b', calculate
% inferred temperature profile
Ta(1) = Ta_data(1);
Tb(1) = Tb_data(1);
for i = 2:k-2
    Ta(i) = 1/(a_coe(10)+a_coe(11)*Ta(i-1)+a_coe(12)*Ta(i-1).^2)*...
        ((a_coe(1)+a_coe(2)*Ta(i-1)+a_coe(3)*Ta(i-1).^2)*Pin_data(i-1)...
        -(a_coe(4)+a_coe(5)*Ta(i-1)+a_coe(6)*Ta(i-1).^2)*(Ta(i-1)...
        - Ts_data(i-1))-(a_coe(7)+a_coe(8)*Ta(i-1)+a_coe(9)*Ta(i-1).^2)...
        *(Ta(i-1)- Tb(i-1)))*(t(i)-t(i-1)) + Ta(i-1);
    Tb(i) = 1/(b_coe(4)+b_coe(5)*Tb(i-1)+b_coe(6)*Tb(i-1).^2)*...
        ((a_coe(7)+a_coe(8)*Ta(i-1)+a_coe(9)*Ta(i-1).^2)*(Ta(i-1)...
        - Tb(i-1))-(b_coe(1)+b_coe(2)*Tb(i-1)+b_coe(3)*Tb(i-1).^2)...
        *(Tb(i-1)- Ts_data(i-1)))*(t(i)-t(i-1)) + Tb(i-1);
end

Ta = Ta';
Tb = Tb';

% plot Ta, Tb vs time
figure(2)
```

```
plot(t(1:k-2), Ta, 'color', [.27 .45 .64],'LineWidth', 4)
set(gca, 'FontSize', 24);
title('Calibration Ta')
xlabel('time (s)')
ylabel('Ta (K)')
hold on
plot(t, Ta_data, 'color',[.88 .42 .15] , 'LineWidth', 4)
legend('Ta inffered','Ta data')
plot(t(1:k-2), Tb, 'color', [.27 .45 .64],'LineWidth', 4)
plot(t, Tb_data, 'color',[.88 .42 .15] , 'LineWidth', 4)


for i = 1:k-2
    Pin_inf(i) = (dTa_data(i)*
(a_coe(10)+a_coe(11)*Ta_data(i)+a_coe(12)...
        *Ta_data(i).^2) + (a_coe(4)+a_coe(5)*Ta_data(i)+a_coe(6)...
        *Ta_data(i).^2)*(Ta_data(i) - Ts_data(i))+(a_coe(7)+a_coe(8)*...
        Ta_data(i)+a_coe(9)*Ta_data(i).^2)*(Ta_data(i) - Tb_data(i))...
        /(a_coe(1)+a_coe(2)*Ta_data(i)+a_coe(3)*Ta_data(i).^2);
end
Pin_inf = Pin_inf';

figure(3)
plot(t(1:k-2), Pin_inf, 'color', [.27 .45 .64], 'LineWidth', 4)
set(gca, 'FontSize', 24);
title('Calibration Pin')
xlabel('time (s)')
ylabel('Pin (W)')
hold on
plot(t, Pin_data, 'color',[.88 .42 .15] , 'LineWidth', 4)
legend('Pin inffered','Pin data')

%% Apply coefficients into the sample run data to infer the enthalpy
% read chemical run data
[num,txt,raw] = xlsread('Chemical run');
time = raw(2:end, 2);
Ta_data = raw(2:end,3);
Tb_data = raw(2:end,4);
Ts_data = raw(2:end,5);
Pin_data = raw(2:end, 6);

t = downsample(cell2mat(time),downsize,1);
Ta_data = downsample(cell2mat(Ta_data),downsize,1) + 273;
Tb_data = downsample(cell2mat(Tb_data),downsize,1) + 273;
Ts_data = downsample(cell2mat(Ts_data),downsize,1) + 273;
Pin_data = downsample(cell2mat(Pin_data),downsize,1);

clear num dTa_data Pin_inf
k = numel(t);

for i = 1:k-2
    dTa_data(i) = (Ta_data(i+1)-Ta_data(i))/(t(i+1)-t(i));
end

% calculate inferred total power
```

```
for i = 1:k-2
    Pin_inf(i) = (dTa_data(i)*
(a_coe(10)+a_coe(11)*Ta_data(i)+a_coe(12)...
        *Ta_data(i).^2) + (a_coe(4)+a_coe(5)*Ta_data(i)+a_coe(6)...
        *Ta_data(i).^2)*(Ta_data(i) - Ts_data(i))+(a_coe(7)+a_coe(8)*...
        Ta_data(i)+a_coe(9)*Ta_data(i).^2)*(Ta_data(i) - Tb_data(i)))/...
        (a_coe(1)+a_coe(2)*Ta_data(i)+a_coe(3)*Ta_data(i).^2);
end

%% Calculate Psample_inf

% calculate inferred power from the sample
for i = 1:k-2
    Psample_inf(i) = (dTa_data(i)*
(a_coe(10)+a_coe(11)*Ta_data(i)+a_coe(12)...
        *Ta_data(i).^2) + (a_coe(4)+a_coe(5)*Ta_data(i)+a_coe(6)...
        *Ta_data(i).^2)*(Ta_data(i) - Ts_data(i))+(a_coe(7)+a_coe(8)*...
        Ta_data(i)+a_coe(9)*Ta_data(i).^2)*(Ta_data(i) - Tb_data(i)))-...
        (a_coe(1)+a_coe(2)*Ta_data(i)+a_coe(3)*Ta_data(i).^2)*Pin_data(i);
end

% plot inferred heater power and inferred sample power
figure(4)
plot(t(1:k-2), Pin_data(1:k-2), 'color',[.88 .42 .15] , 'LineWidth', 4)
set(gca, 'FontSize', 24);
title('Fuel run Pin')
xlabel('time (s)')
ylabel('Pin (W)')
hold on
plot(t(1:k-2), Pin_inf, 'color',[.27 .45 .64] ,'LineWidth', 4)
legend('Pin data', 'Pin inffered')

figure(5)
plot(t(1:k-2), Psample_inf(1:k-2), 'color',[.88 .42 .15] , 'LineWidth', 4)
set(gca, 'FontSize', 24);
title('Inferred Sample Power')
xlabel('time (s)')
ylabel('Pin (W)')



%% define Levenberg Marquardt method as a function
function a_coe = LMmethod(x, y, func, a, a_coe)

% x is the independent varialble of sample data
% y is the dependent variable of sample data
% a is the vector of coefficient a
% a_coe is the value of the initial guess of a,the out put a_coe is the...
% optimized a
% func is the function that relates y, x and a

%define constants
lambda = 1e-3;
k = numel(a_coe);
I = eye(k);
```

```
iteration = 0;
for i = 1:k
    beta = sum(diff(func, a(i)).*(y - func));
    beta_new = matlabFunction(beta, 'Vars', {[a]});
    % the result has 'in1' as input, need to change it back to 'a'
    str = func2str(beta_new);
    newstr = strrep(str, 'in1', 'a');
    beta_new = str2func(newstr);
    B{i} = beta_new;
end

% define Jacobian matrix
for  i = 1:k
    beta = sum(diff(func, a(i)).*(y - func));
    for j = 1:k
        alpha = -diff(beta, a(j));
        alpha_new = matlabFunction(alpha, 'Vars', {[a]});
        % the result has 'in1' as input, need to change it back to 'a'
        str = func2str(alpha_new);
        newstr = strrep(str, 'in1', 'a');
        alpha_new = str2func(newstr);
        J{i,j} = alpha_new;
    end
end

% define func back to a anonymous function
func_new = matlabFunction(func, 'Vars', {[a]});
str = func2str(func_new);
newstr = strrep(str, 'in1', 'a');
func_new = str2func(newstr);

%start loop for extimating values of a
while 1
    % calculate J matrix
    for i = 1:k
        for j = 1:k
            J_value(i,j) = J{i,j}(a_coe);
        end
    end

    LSQ = sum((y - func_new(a_coe)).^2);
    J_value = J_value + lambda*I;

    for i = 1:k
        f(i) = B{i}(a_coe);
    end

    da = inv(J_value)*f.';
    a_coe_new = a_coe + da.';

    NewLSQ = sum((y - func_new(a_coe_new)).^2);
    % compare NewLSQ and LSQ
    if NewLSQ <= LSQ
        a_coe = a_coe_new;
```

```
        lambda = lambda/10;
    else
        lambda = lambda*10;
    end
    % determine where to stop
    if abs(NewLSQ - LSQ) < 0.0000000001
        break
    end
    abs(NewLSQ - LSQ);
    iteration = iteration + 1
end

end
```